Fall 12-18-2014

Modal Characterization and Structural Dynamic Response of a Crane Fly Forewing

Jose E. Rubio
University of New Orleans, jerubio@uno.edu

Modal Characterization and Structural Dynamic Response of a Crane Fly Forewing

A Thesis

Submitted to the Graduate Faculty of the
University of New Orleans
in partial fulfillment of the
requirements for the degree of

Master of Science
in
Engineering-Mechanical
Solid Mechanics

by

José Enrique Rubio

B.Sc., University of New Orleans, 2012

December, 2014

Dedicated to my parents for their love, support, and encouragement

Acknowledgement

I would like to thank my major professor Dr. U. Chakravarty for giving me the opportunity to be part of his research team. Such opportunity has definitely helped me to gain on-hands research experience and to enhance my ability to work independently and think critically. Most importantly, without Dr. Chakravarty's knowledge, motivation, and mentorship finishing this study would not have been possible.

I am extremely grateful to Dr. P. Schilling for being my undergraduate advisor and serving as a committee member for my master's thesis. His constant advices since the beginning of my undergraduate career and his valuable input towards the completion of this research have been a keystone for my personal and professional development throughout these years.

I would also like to extend my thanks to Dr. M. Guillot for serving as a committee member for my thesis. His recommendations and support were fundamental to improve the quality of this manuscript.

I would like to express my gratitude to my colleagues Manohar Chidurala and Pratik Sarker for their constant help in building the computational models. Also, I extend my thanks to William Miller for his assistance on the scanning of the specimen and to Claude Zeringue for his help in the construction of the experimental setup.

Lastly, I feel indebted to my family for their endless support and encouragement. Thanks for always being there for me.

Table of Contents

Nomenclature

A – Surface area

C_D – Coefficient of drag

C_L – Coefficient of lift

c – Chord length

D – Total derivative

E – Modulus of elasticity

F_D – Drag force

F_L – Lift force

g – Gravity or buoyancy force

h – Thickness of shell

L – Characteristic length

l – Length of flat plate

n – Normal direction to a referenced surface

p – Pressure

q – Distributed load

Re – Reynolds number

S_V – Von-Mises stress

s – Span length

t – time

U – Deformation magnitude

U_x – Deformation component in *x*-direction

U_y – Deformation component in *y*-direction

U_z – Deformation component in *z*-direction

V – Velocity

V_∞ – Freestream velocity

$\vec{V}$ – Velocity vector

v_x – Velocity component in *x*-direction

v_y – Velocity component in *y*-direction

v_z – Velocity component in *z*-direction

w – Out of plane or transverse deflection

x – Cartesian coordinate

y – Cartesian coordinate

z – Cartesian coordinate

Greek symbols

δ – Boundary layer thickness

θ – Angle of attack

λ_{ij} – Kronecker's delta function

μ – Dynamic or absolute viscosity

ρ – Density

τ_{ij} – Stress tensor

ν – Poisson's ratio

υ – Kinematic viscosity

Ω – Shell domain for vibration mathematical model

ω – Frequency

Symbols

$\vec{\nabla}$ – Gradient vector

∇^4 – Biharmonic operator

∂ – Partial derivative or differential element

$\partial\Omega$ – Clamped edge of shell

$\partial\zeta$ – Surface of immersed body

List of Figures

List of Tables

Abstract

This study describes a method for conducting the structural dynamic analysis of a crane fly (family *Tipulidae*) forewing under different airflow conditions. Wing geometry is captured via micro-computed tomography scanning. A finite element model of the forewing is developed from the reconstructed model of the scan. The finite element model is validated by comparing the natural frequencies of an elliptical membrane with similar dimensions of the crane fly forewing to its analytical solution. Furthermore, a simulation of the fluid-structure interaction of the forewing under different airflows is performed by coupling the finite element model of the wing with a computation fluid dynamics model. From the finite element model, the mode shapes and natural frequencies are investigated; similarly, from the fluid-structure interaction, the time-varying out-of-plane deformation, and the coefficients of drag and lift are determined.

Keywords: Fluid structure interaction, finite element model, crane fly, structural response, aerodynamics, MAVs.

CHAPTER 1. INTRODUCTION

Insects are by far the oldest, most numerous, and smallest flying organisms which have had an important evolutionary success due to their superlative maneuverability during low-speed flight. Flying insects, in general, experience highly elastic deformations in their wings during the flapping cycle to create the aerodynamic forces that allow them to hover and to maneuver. The study of flapping flight has captivated and motivated scientists to perform quantitative and qualitative descriptions of the kinematics and the mechanical and aerodynamic principles that govern insect flight. The significance of such detailed studies is the potential application of these aerodynamic principles into engineered devices, e.g. biologically inspired micro air vehicles (MAVs). Moreover, in order to successfully biomimic the aerodynamic performance of insects, the MAVs must have a robust design with efficient, optimized wing structures such as those from insects. This study concentrates on characterizing the structural dynamic response of the crane fly, an insect, in vacuum and under different airflow conditions. Specifically, the deformation and aerodynamic performance of the crane fly forewing are investigated.

1.1. Flow over Immersed Bodies

External flow past an object involves different fluid mechanics phenomena. For a given shaped object, the characteristics of the flow depend strongly on various parameters such as the size and orientation of the object, the speed of the fluid, and the fluid properties. Furthermore, the character of the flow is governed by different dimensionless parameters. For typical external flow, the most important parameter is the Reynolds number which is defined as the ratio of the inertial forces to the viscous forces and mathematically expressed in Eq.1.1. [1]

$$\mathrm{Re} = \frac{\rho V_\infty L}{\mu} \tag{1.1}$$

In general, if the Reynolds number is small, the inertia effects are relatively small compared to the viscous effects. Moreover, if the Reynolds number is large, the region in which the viscous effects are dominant is allocated very close to the surface of the immersed body while the rest of the flow field is dominated by inertial effects. The region in which the viscous effects dominate is known as the boundary layer and its thickness increases in the direction of flow. Furthermore, within the boundary layer, the velocity changes from the freestream velocity to zero velocity on the surface of the immersed body. The reason for the existence of this boundary layer is that the viscosity of the fluid is not zero; consequently, the fluid must stick to the solid surface, this is known as the no-slip boundary condition. This thin boundary (thin compared to the length of the object) is responsible for the production of the lift and the drag forces and it is approximately represented in Fig 1.1.

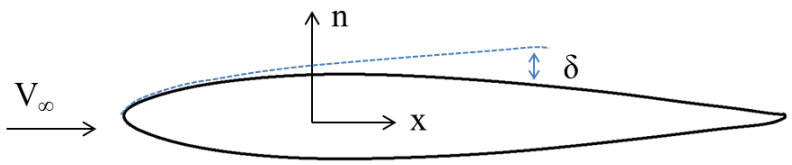

Figure 1.1. Boundary layer representation

When a fluid moves over an immersed body, an interaction occurs which can be described in terms of the forces at the fluid-body interface. The resultant force in the direction of the flow is called drag; while the resultant force in the normal direction to the flow is termed lift. Referring to Fig.1.1, the lift and the drag forces are mathematically defined in Eqs. 1.2 and 1.3, respectively [1].

$$F_D = \int p_x dA \tag{1.2}$$

$$F_L = \int p_n dA \tag{1.3}$$

The generation of these two forces is directly related with the pressure distribution along the surface area of the immersed body. In general, when a fluid flows past a non-symmetric object, the pressure field is not uniform. As discussed previously, a relatively thin boundary layer is developed along each of the surfaces of the immersed body; within this layer, the component of the pressure gradient in the direction of the flow is not zero, while the component in the normal direction is negligibly small. This pressure gradient is caused by the variation of the freestream velocity across the boundary layer and it generates the so-called drag and lift forces. Alternatively, the drag and lift forces can be defined in terms of dimensionless parameters called the drag and lift coefficients which are defined in Eqs. 1.4 and 1.5, respectively [1].

$$C_D = \frac{F_D}{\frac{1}{2}\rho V_\infty^2 A} \tag{1.4}$$

$$C_L = \frac{F_L}{\frac{1}{2}\rho V_\infty^2 A} \tag{1.5}$$

1.2. Insect Flight Kinematics

An understanding of basic wing terminology is required before proceeding with any further discussion. The morphology of a typical insect wing, presented in Fig. 1.2, has two main features: the leading edge and the trailing edge, which refer to the foremost and rear edge of the wing, respectively. Furthermore, the wing span is referred as the distance from the tip of the wing to the root of the wing where it intersects with the thorax of the insect. On the other hand, the chord length is defined as the distance between the trailing edge and the corresponding point in the leading edge.

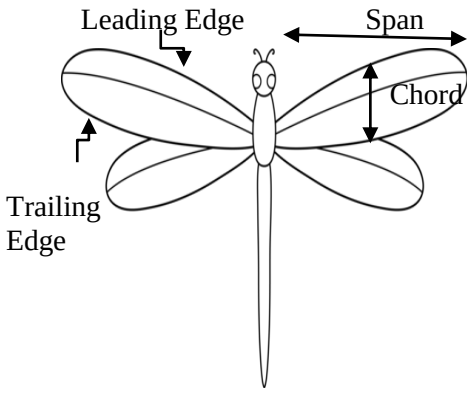

Figure 1.2. Insect wing terminology

The flapping cycle of an insect is conformed of two translational phases: downstroke and upstroke; and two rotational stages: pronation and supination, all of them depicted in Fig. 1.3. Downstroke and upstroke occur when the wing translates over the air at a higher angle of attack. Moreover, wing pronation occurs during the transition from upstroke to downstroke and it consists in the inward rolling of the wing towards the thorax of the insect; on the other hand, supination occurs during the transition from downstroke to upstroke and it consists in the outward rolling of the wing towards the torso of the insect [2, 3].

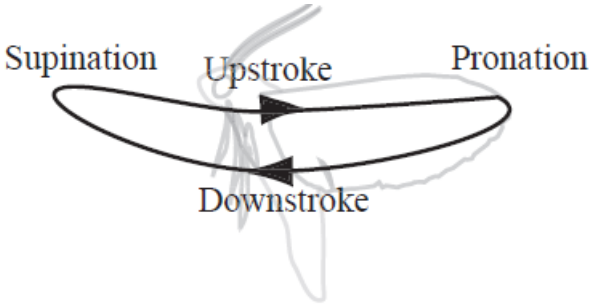

Figure 1.3. Flapping cycle of insects [3]

Identifying the manner in which insect wings provide the needed lift for flight has been extremely difficult. Their small scale and rapid wing-beat make experimental measurements problematic and collecting data from tethered insects may often yield data based on unnatural

movements. However, some principles have been identified using mechanical models that are matched to that of an actual insect, ensuring that the governing fluid dynamic phenomena are conserved. These models together with advanced experimental setups such as high-speed cameras, digital image correlation software, and particle image velocimetry systems have made possible the identification and analysis of the different unsteady mechanisms that govern the kinematics of insect flight.

It is essential to remark that insects do not create the required lift forces by simply flapping their wings since the effects of the downstroke would be aerodynamically cancelled out by the equivalent ones from the upstroke [4]. Instead, insects generate the needed lift and thrust by experiencing unsteady aerodynamic mechanisms coupled with highly elastic deformations in their wings derived from the aerodynamic loading from flapping flight. Three unsteady mechanisms have been identified in the aerodynamics of insect flight, although the occurrence of all the three of them is not guaranteed in every insect. The first mechanism, the clap and fling mechanism shown in Fig.1.4, consists of raising the wings so the tips touch dorsally before they pronate. The leading edges touch each other or "clap" before the trailing edges, progressively closing the gap between them and forming a shape similar to a vertical plate. As the wing presses together closely, the opposing circulations of each of the wings are canceled out each other. The wings are then quickly pronated with the leading edges "fling" apart, creating a low-pressure region between them that causes the gap to be filled with entering air, consequently providing an initial momentum and a vortex of air [3, 4]. Collectively, the clap and fling mechanism results in a modest, but significant, lift enhancement. The second well-identified unsteady mechanism in insect flight is the delayed stall and it is shown in Fig. 1.5. As the wing increases its angle of attack, the fluid stream going over the wing separates as it crosses the leading edge but reattaches

before it reaches the trailing edge. In such cases, a leading edge vortex occupies the separation zone above the wing. If the wing translates at a higher angle of attack, the leading edge vortex grows in size until flow reattachment is no longer possible. As a result, there is a drop in the lift and the wing is said to have stalled. For several chord lengths prior to the stall, the presence of the attached leading edge vortex produces very high lift coefficients, a phenomenon termed "delayed stall" [3, 4] . Delayed stall has been highly associated with the deformation experienced by insects at low Reynolds number. The third unsteady mechanism is the wake capture and rotational circulation. The former allows the wing to take advantage of the wake created by the previous stroke while the latter allows an upward lift to be generated when the wing's own rotation creates air circulation at the end of the stroke [3, 4].

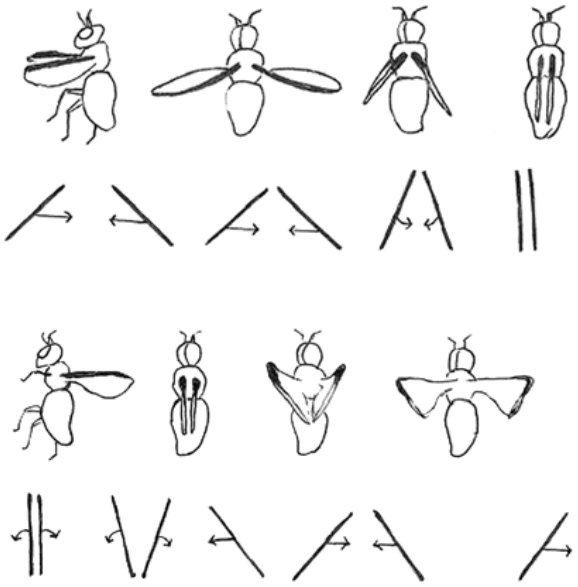

Figure 1.4. Clap mechanism (top) and fling mechanism (bottom) [3, 4]

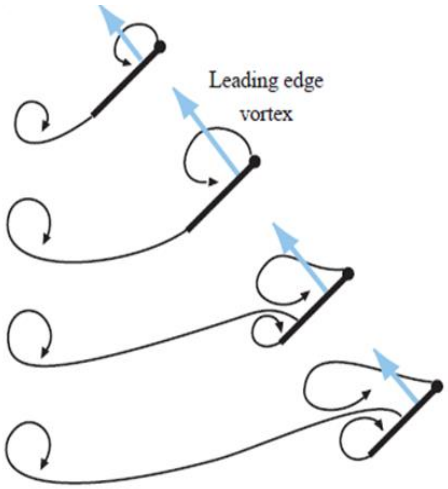

Figure 1.5. Delayed stall and wake capture mechanism [3]

1.3. Micro Air Vehicles

Understanding the role of wing flexibility in producing unsteady aerodynamic forces and mechanisms that enable flapping flight is fundamental for the potential emulation of flapping flight in man-made manufactured devices. Moreover, characterizing the structural response of insect wings to dynamic loading is seen as the keystone for the development of the new generation of high-performance and aerodynamically efficient MAVs.

MAVs are autonomous, lightweight, small-scale flying devices with a maximum wing span of 15 cm and a maximum flying speed of approximately 15 m/s as detailed in Table 1.1. Interest in the design of these aerial devices has immensely grown over the last years due to their potential to operate in remote or otherwise hazardous locations where they may perform a variety of tasks, including but not limited to, reconnaissance, surveillance, and safety inspection. To accomplish the aforementioned tasks, the wings of MAVs should be aerodynamically efficient, optimized structures; such as the wings found in different insects. Currently, extensive research is being done to design biologically inspired MAVs that mimic the superlative maneuverability characteristics during low-speed flight mastered by insects.

Table 1.1.MAVs design requirements as outlined by the Defense Advanced Research Projects Agency (DARPA) [5, 6]

Specifications	Requirements	Details
Size	<15.24 cm	Maximum dimension
Weight	~100 g	Objective gross takeoff weight (GTOW)
Range	1 to 10 km	Operational range
Endurance	60 min	Loiter time on station
Altitude	<150 m	Operational ceiling
Speed	15 m/s	Maximum flight speed
Payload	20 g	Mission dependent
Cost	$1500	Maximum cost, 2009 USD

1.4. Literature Survey

Detailed research on the field of aerodynamics of insects traces back from about 40 years ago. A pioneer work on this field was presented by Ellington through his compendium of studies about the aerodynamics of hovering insect flight [7–12]. Ellington re-examined and questioned the conventional quasi-steady assumption proposed by Weis-Fogh [13, 14], which assumed that the instantaneous forces on a flapping wing were equivalent to those for steady motion and concluded that the aforementioned theory lacked of high fidelity evidence. First, Ellington analyzed the principles and the validity of the quasi-steady assumption to conclude that further studies were required to confirm such theory [7]. Consequently, he investigated and presented a list of morphological and kinematic data for a variety of insects [8, 9]; which he then used to offer an aerodynamic interpretation of the kinematics of insect wings and a discussion on the possible roles of different aerodynamic mechanisms [10]. From the previous study, it was determined that leading edge separation bubbles were prominent features in insect flight causing flow to separate at the leading edge and then to reattach downstream to the upper wing surface; consequently, producing a region of recirculating flow which improved the lift at low Reynolds number. Lastly, the new data about aerodynamic mechanisms was combined for an analysis of

the lift and power requirements of hovering flight and a development of a vortex theory for lift generation in insects [11, 12].

The previously described studies provided a novel insight about the aerodynamics of insect wings and led to the development of research that concentrated on characterizing the functional morphology of insect wings, outlining the principles of the biomechanics of insect flight, and describing on detail the load bearing capacity of insect wings [15–18]. Ennos and Wootton [15] and Wotton [16, 17] experimentally investigated various features of different insect species including their morphology, flight mechanics, and control behavior. Their work suggested that the wings cambered and twisted slightly due to inertial forces. Furthermore, they determined that both bending and deformation were highly dependent on the structure and venation morphology of the wing and that these altered the direction and magnitude of aerodynamic force production. Specifically, the bending and the deformation enhanced thrust production by creating an asymmetric force between half-strokes and increased lift production by allowing wings to twist and to generate upward force throughout the stroke cycle. Quite similar findings were reported by Yin and Luo [18] who simulated the fluid-structure interaction (FSI) in hovering flight to investigate the effect of inertia and fluid deformation on hovering performance. They reported that both inertia-induced and flow-induced deformation could enhance the lift generation of the wing.

Wing flexibility plays an important role when characterizing the deformation experienced by insects during aerodynamic loading; therefore, different experimental studies have directed their objectives towards finding the relationship that best describes the dependence of wing deformation with respect to wing flexibility. Combes and Daniel [19, 20] addressed the relationship between venation pattern and wing flexibility by measuring the flexural stiffness of

wings due to an applied point load and quantifying wing venation variation in different insect species. They concluded that flexural stiffness declined sharply from wing base to tip and from the leading to the trailing edge. Ishihara et al. [21] studied the two-dimensional (2-D) FSI in *Dipterian* flapping flight; specifically, they concentrated on the passive pitching due to wing torsional flexibility. It was demonstrated that insects kept the high angle of attack during its translation and that the pitch angle rotated at the stroke reversal. Furthermore, they concluded that it is especially important that the wing begins to twist before it changed its flapping direction so that it could generate the required lift.

Several studies have used numerical methods, such the finite element (FE) method, to simulate wing structures and compare their results with experimental data. Combes and Daniel [22] addressed the relative contributions of aerodynamic and inertial-elastic forces to wing bending in a *Manduca sexta* forewing by using experimental data and a FE model. Their results suggested that a damped FE model, with realistic forces applied at the base, could be successful in predicting the overall pattern and the magnitude of the insect wing deformation during flight, independently of aerodynamic calculations. Sims et al. [23] conducted an experimental structural analysis of a dragonfly, *Manduca sexta,* forewing by collecting frequency data using laser vibrometry in air and in vacuum and comparing the results with a computational model. They concluded that camber was an important structural property for the *Manduca sexta.* Jongerius and Lentink [24] conducted a similar structural analysis directed to determine how the wings of a dragonfly, *Sympetrum vulgatu,* carried the aerodynamic and inertial loads during regular insect flight using an approximated mathematical inertial load model. Rubio et al. [25] investigated the structural response of a symmetric sail-like insect wing model inspired from a crane fly specimen.

The progress on the characterization of insect flight has foster a new multi-disciplinary collaboration, between biologists who seek to understand how the aerodynamic loads are related to insect physiology and evolution, and engineers who aspire to build micro-robotic insects using these principles. This trend has led to different investigations concentrating on the biomimetic of insect flight characteristics in MAVs. Ellington [26] studied the aerodynamic characteristics of insects applicable to MAVs. He presented different design characteristics of insect-based flying devices and estimates of the mass they could support, their mechanical power requirement, and their maximum flight speeds over a wide range of sizes and frequencies. His work suggested that for the simplest implementation of insect features into MAVs a simple sail-like construction would suffice with features such as a stiff leading edge supporting a membrane and independent adjustment of both the flapping amplitude and the mean flapping angle.

Further research efforts have been done in smart materials that could potentially biomimic the structural characteristics of insect wings. Chakravarty [27] investigated the vibration characteristics of biologically inspired wings fabricated from composite polyester materials. He concentrated on investigating the effect of added mass, aerodynamic pressure, and damping on the vibration characteristics of such wings. An inversely proportional relationship was found between the magnitude of the natural frequency and the added mass. Moreover, Chakravarty and Albertani [28] investigated the effects of aerodynamic loads on the modal characteristics on a biologically inspired wing fabricated from a hyperleastic membrane. They determined that the natural frequency of a membrane increased with pre-strain level and that the damping of air had minimal effect on the natural frequencies of the wing but assisted on reducing the out-of-plane modal amplitude of vibration. Wu et al. [29] studied the structural properties of biologically inspired insect wings by measuring the full-field deformation and flow around six

pairs of hummingbird-shaped membrane wings of different properties at atmospheric pressure and in vacuum. They described the aeroelastic behavior of the wings and visually explained the relationship between flexibility and thrust production. Their research supported that wing deformation was a vital feature for generating aerodynamic thrust in insects indicating the important role of flexibility in bio-inspired wings.

1.5. Motivation and Objective of Study

The special attention drawn to biomimic insect wings which could potentially be implemented into MAVs is the motivation for this study. In order to develop structures that could demonstrate the same excellent structural response of insect wings, one must first be able to thoroughly analyze the aerodynamic behavior of insect wing in vacuum and under airflow conditions and then translate such behavior into the engineered structure. Few studies, to the knowledge of the author, have been developed to analyze the FSI of insect wings to quantify the structural dynamic response of the wings in terms of deformation and aerodynamic variables, namely lift and drag forces. Therefore, this manuscript presents a numerical method for investigating the structural dynamic response of a crane fly forewing, an insect in the family *Tipulidae*. The aim of this study can be decomposed into two sections:

1) **Characterization of the external and internal morphologies of the crane fly forewing:** The inherent scale of insects makes the accurate description of the structure of the wing a cumbersome task. Furthermore, insect wings are characterized by complex wing patterns that intersect at multiple times and that are hold together by a thin membrane. Given this complexity, a wing sample is digitally captured using a micro-computed tomography (micro-CT) scanner which is the most advanced three dimensional (3-D) microscopy method. Through dedicated measurements from the reconstructed wing

model the external and internal morphologies of the wing are subsequently transferred into a FE model.

2) **Investigation of the structural dynamic response of the crane fly forewing:** Quantifying the instantaneous deformation on insect wings helps determine the direction and magnitude of fluid-dynamic forces generated by the inertial and aerodynamic load; therefore, being able to predict large, dynamic shape changes is essential for developing a comprehensive understanding of insect flight. The FE model, developed from the micro-CT scan, is used to perform a complete modal analysis of the forewing in vacuum. Similarly, FSI simulations under steady and unsteady conditions at low freestream velocities are performed by coupling the FE model of the forewing with a computational fluid dynamics (CFD) model. The deformations and aerodynamic coefficients of the forewing are investigated from such simulations.

CHAPTER 2. MATERIALS AND METHODS

2.1. Specimen Characterization

2.1.1. Selection and Description of the Specimen

A crane fly forewing is used for the development of this study. This insect belongs to the family *Tipulidae* [30] which may be recognized by their slender bodies and long, slender legs. Common nicknames for this specimen are “daddy-long-legs”, “golly whopper”, and “mosquito hawk”. The selection basis is rather arbitrary within the framework of insect specimens that are proven to be aerodynamically efficient at low-speed flight and hovering [8]. A picture of a typical adult crane fly is presented in Fig. 2.1 (left) and a summary of morphological and kinematic parameters, which are averaged from different specimens in references [23, 24], is described in Table 2.1. It is noteworthy the size scale of the crane fly with a miniature wing span in the order of 10^{-3} m. This scale can also be seen in Fig. 2.1 (right) which presents a dried specimen of a crane fly next to a millimeter metric scale. Furthermore, it is noticeable the flapping frequency of 45.5 Hz at low-speed flow regimens from the crane fly which is reasonable as small insects tend to have higher flapping frequencies.

Figure 2.1. Typical adult crane fly (left) and metric scale for an adult crane fly (right)

Table 2.1. Morphological and kinematic parameters for the crane fly [23, 24]

Parameter	Value
Wing span length (per wing)	12.7 mm
Averaged chord length	2.37 mm
Wing pair area	59 mm^2
Wing pair mass	0.000245 g
Total insect mass	0.0114 g
Stroke angle	123°
Flapping frequency	45.5 Hz
Reynolds number	$20 < Re < 200$

2.1.2. Specimen Evaluation

The crane fly forewing is a rather complex structure as it can be seen from Fig. 2.2. There are several veins, many of which intersect multiple times, attached to a membrane. Moreover, a meticulous visual inspection may reveal different vein thicknesses but surely their magnitudes cannot be determined from this inspection. Prior proceeding with developing any FE model, a high-fidelity structural characterization of the wing is required. Because of the small scale of the specimen and the complexity of the wing structure, the number of instruments and techniques capable of providing accurate quantitative description of the external and internal morphologies of the crane fly forewing are limited. One solution to this intrinsic problem is to characterize the structure of the wing using micro-CT scan, the most advanced non-intrusive 3-D microscopy technique.

Figure 2.2. Crane fly forewing sample

2.2. Micro-CT Scan

2.2.1. Background

To analyze the structural dynamic response of the crane fly forewing, a 3-D characterization of the wing structure is required. Conventional optical microscopy allows visualizing 2-D images of the specimen surface. However, in most of the cases, a conclusion about the 3-D structure cannot be made on the basis of 2-D information. One alternative to obtain 3-D information of the structure of the specimen is to cut the specimen into very thin slices, then use an optical microscope to visualize and analyze the structure, and finally interpolate the 2-D information into the 3-D model. However, this method is not only very cumbersome but also unreliable since the structure of the specimen itself can be altered by the intrusive preparation technique, especially with fragile structures such as insect wings. A more accurate non-intrusive method is required to characterize the internal structure; therefore, micro-CT scanning is selected as the most appropriate method to digitize the wing sample since it provides a complete and precise representation of the 3-D structure of the wing.

2.2.2. 3-D X-Ray Microscopy Principle

3-D X-ray microscopy allows reconstructing, visualizing, and measuring complete 3-D structures without sample preparation. The principle behind computed tomography is the interaction of ionizing radiation absorption between an X-ray source and a sample subjected to the scan. A CT image is created by directing X-rays through the slice plane from multiple orientations and measuring their resultant decrease in intensity. The simplest micro-CT scan setup is shown in Fig. 2.3 and it consists of an X-ray source, a sample, and an X-ray detector that measures the extent to which the X-ray signal has been attenuated by the sample. As the X-ray beam penetrates the object, it is exponentially attenuated according to the absorption rate from

the different materials that compose the sample along its path [31]. Furthermore, the actual attenuation not only depends on the density of the sample material but also on the energy spectrum from the X-ray source. To accurately produce a 3-D CT image, a whole set of 2-D projections needs to be collected by a planar detector. Based on multiple angular views acquired while the object rotates, a computer synthesizes a stack of virtual cross-section al slices through the object to build a 3-D digital model [32].

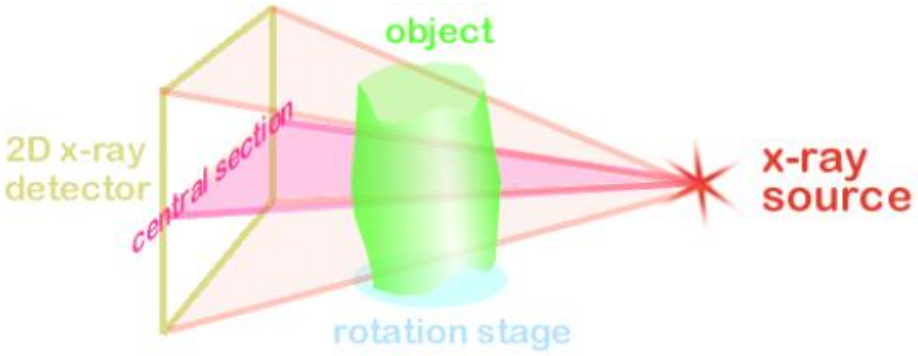

Figure 2.3. Typical micro-CT scan setup

2.2.3. Stages of Micro-CT Scan

To reconstruct a 3-D digital model from a set of 2-D cross-sectional projected images, the following stages are required during a micro-CT scan: acquisition, reconstruction, and transformation from cross-section to image. The next paragraphs present a brief description of the aforementioned stages, leaving algorithm and mathematical details out of the discussion since they are out of the scope of this study.

1) ***Acquisition:*** During the acquisition stage, the sample rotates over 180° or 360° with a fixed rotational step. At each angular position a shadow or projected image is acquired as a 16 bit Tagged Image File Format (TIFF) file [32] by the 2-D detector.
2) ***Reconstruction:*** Using the Feldkamp reconstruction algorithm [33], also known as back projection algorithm, a matrix of raw data containing the attenuation values of the

acquired cross-sectional projected images is generated. This raw data is not yet an image; it is a floating point matrix holding the absorption values from the reconstructed cross-sections.

3) ***Cross-section to image:*** This stage consists of generating the 3-D image from the cross-section slices. The data from the floating point matrix is converted into a gray scale image. The minimum and maximum attenuation are identified and the rest of the values between this range are displayed as halftone. The reconstructed array is shown as a half-tone image of the cross section with linear conversion to 256 grades of gray inside the selected density interval.

2.2.4. Scanning Setup

For this study, a SkyScan 1172 high-resolution micro-CT scanner is used. A crane fly forewing is collected and placed inside the scanner chamber using one of the sample holders. No preparation is required on the sample; however, special care is taken to avoid damage or alteration to the structure of the wing. Using the acquisition software from the scanner, the acquisition settings are adjusted to achieve a good contrast between the different structures of the wing, namely the membrane and the veins. This procedure is quite challenging given the size and inherent transparency of the crane fly forewing, which makes the wing structure hard to appreciate in the preview snapshots. Furthermore, the densities of the membrane and the veins do not differ significantly; therefore, the scanning process is more difficult given that their X-ray absorption rates are very similar.

In general, most of the acquisition settings are determined by trial and error; however, few trends are noticed during this experimental stage. For this application, increasing the energy of the X-rays is not very effective as higher-energy beams of rays are less sensitive to attenuation

contrasts in a specific material; thus, there is not sufficient differentiation, i.e. changes in material density and composition, between features of interest. Furthermore, objects with a low rate of X-ray absorption are scanned more effectively if no filter is present. Filters are commonly flat or shaped pieces of metal such as copper, brass or aluminum, commonly used to absorb the low energy beam of rays in the spectrum. Lastly, a small rotational step for a complete revolution around the specimen is desired due to the asymmetric features of the insect wing. The complete lists of acquisition settings used for the scanning process of the crane fly forewing are presented in Table 2.2.

Table 2.2. Micro-CT scanning setup settings

Parameter	Value
Source voltage	23 kV
Source current	100 μA
Filter	No filter
Object to source	169.420 mm
Camera to source	273.504 mm
Exposure	5400 ms
Rotation step	0.250°
Rotation degrees	360°

2.2.5. Characterization of the External and Internal Morphologies of the Crane Fly Forewing

The structure of an insect wing is evolutionary determined by the need to optimize the production of favorable aerodynamic forces during flight. Fully functional wings are found only in adult insects and their external and internal morphologies are quite unique with some general characteristics that are common for all species. Each of the wings of an insect consists of a thin membrane supported by a number of well-marked veins running along the span- and chordwise direction of the wing and connected to each other by cross-veins. In very small insects, the venation may be greatly reduced. Conversely, in large insects an increase in venation may occur

through the branching of existing veins to produce accessory veins. The structure of an individual vein reflects its role in the production of useful aerodynamic forces by the wing as a whole. On the leading edge of the wing, the longitudinal veins form a rigid structure supporting the wing as it moves through the air. On the other hand, at the tip of the wing the lack of veins of significant diameter creates a flexible region. Furthermore, as shown in Fig. 2.4, the membrane of an insect wing is formed by two layers of cuticle closely apposed; only separated at the locations where the veins are formed. Moreover, the cuticle surrounding the veins becomes thickened to provide strength and rigidity to the wing [34].

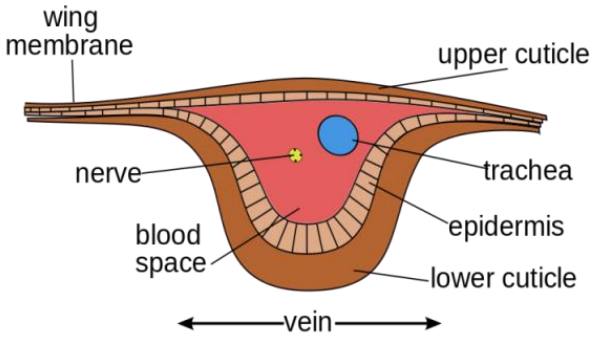

Figure 2.4. Typical internal morphology of an insect wing [34]

The geometry and structure of the crane fly forewing can be accurately described from the reconstructed model of the micro-CT scan. The final parameters of this model are within expected values when compared to the experimental ones presented in Table 2.3. Furthermore, Fig. 2.5 presents a front view of the reconstructed forewing where the membranes and the veins are clearly distinct with different attenuation gray scales. As expected, the venation pattern presents a darker gray scale compared to the one from the membrane. Similarly, the thick veins have a darker gray scale than the one from the thin veins which almost matches the corresponding one of the membrane.

Table 2.3. Final dimensions of the reconstructed model

Parameter	Reconstructed model value	Experimental value [18, 21]
Pixel size	5.3507 μm × 5.3507 μm	--
Average chord length	3.007 mm	2.37 mm
Span length	13.86 mm	12.7 mm

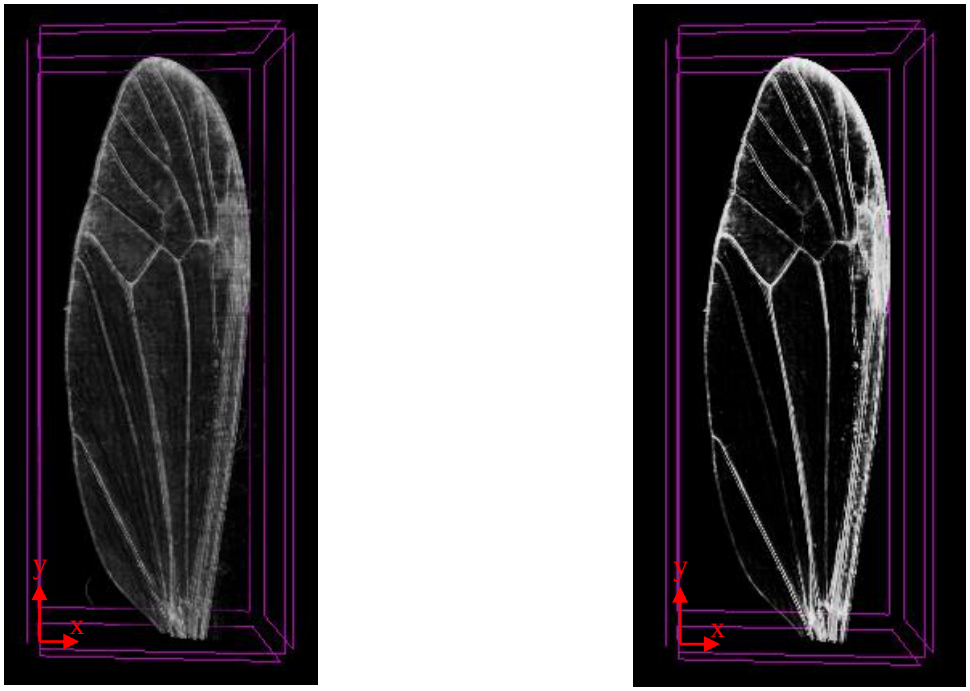

Figure 2.5. Reconstructed model of the crane fly forewing from the micro-CT scan at two different attenuation levels

An interesting structure is observed during the analysis of the internal morphology of the crane fly forewing. Figures 2.6 and 2.7 present images of the cross-section at approximately half the span length of the wing. From these figures, two separated thin layers of cuticle are observed. This gap between these two layers it to some extent inaccurate since insect wings are formed by two layers of cuticle which are very close together, only separated at the locations where the veins are formed, as presented in Fig. 2.4. Nevertheless, this phenomenon is explained by having

used a dry specimen in which the two layers of cuticle are separated. Therefore, the total thickness of the membrane is calculated by averaging the thicknesses of these two layers. Furthermore, using the sliced cross-sectional images, the different diameters of the insect veins with their respective wall thicknesses are accurately determined.

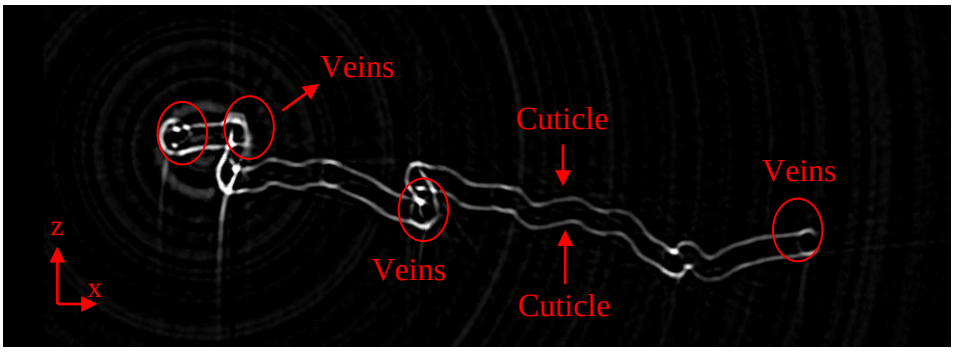

Figure 2.6. 2-D cross-sectional image for the identification of the veins

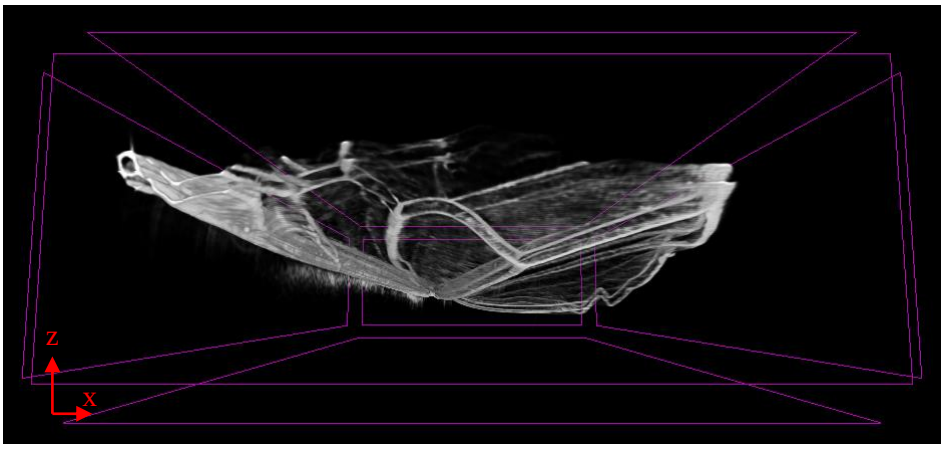

Figure 2.7. Sliced cross-section from the reconstructed 3-D model

2.3. Computational Model

2.3.1. Finite Element Model

2.3.1.1. FE Geometry Construction

The commercially available FE analysis package Abaqus 6.12 [35] is used to develop an Abaqus/Standard FE model. The FE model is developed considering the curvature in *z*-direction

to be much smaller than the spanwise *y*-direction, as seen on the scanned model. The FE model is composed of two parts: membrane and veins.

To determine the dimensions of the contour of the wing, computational measurements of the chord length of the wing are extracted along a central vertical axis for every 0.1605 mm (30 pixels) using the SkyScan CT Analyzer software V. 1.13.2.1 and the 2-D cross-sectional images. The measurements are written into a data file which is then imported into Abaqus 6.12. The dimensions of the FE model are approximately 3.007 mm in the chordwise *x*-direction and 13.86 mm in the spanwise *y*-direction, which fairly agrees with the dimensions of the reconstructed model and with the measurements of the forewing of a crane fly reported by Ishihara et al. [21]. Membrane thickness is manually measured and assumed to be constant throughout the entire wing. Furthermore, two sections of different vein thicknesses are identified through the scan measurements and consequently developed in the FE model to take into account the variation of the stiffness along the wing. The resolution of the scan allows for the identification of only two diameters of veins thicknesses. Lastly, the veins are assigned a tubular profile as observed through the computational measurements and confirmed by Agrawal et al. [36]. Table 2.4 presents a summary of the dimensional parameters of the FE Model.

Table 2.4. Geometric parameters of the FE model

Parameter	**Value**
Span length	13.86 mm
Average chord length	3.01 mm
Membrane thickness	0.016 mm
Thick vein outer diameter	0.11 mm
Thick vein wall thickness	0.04125 mm
Thin vein outer diameter	0.08 mm
Thin vein wall thickness	0.03 mm

2.3.1.2. FE Mesh Description

The membrane is modeled as a 3-D homogeneous shell with a constant thickness and it is meshed using S4R (4-node general-purpose shell) type of element. These types of elements are ideal to model structures in which one dimension, the out-of-plane thickness, is significantly smaller than the other dimensions. Conventional shell elements use this condition to discretize a body by defining the geometry at a reference surface. In this case the thickness is defined through the section property definition. Furthermore, these types of elements have displacement and rotational degrees of freedom. The membrane part and its respective mesh are shown in Fig. 2.8.

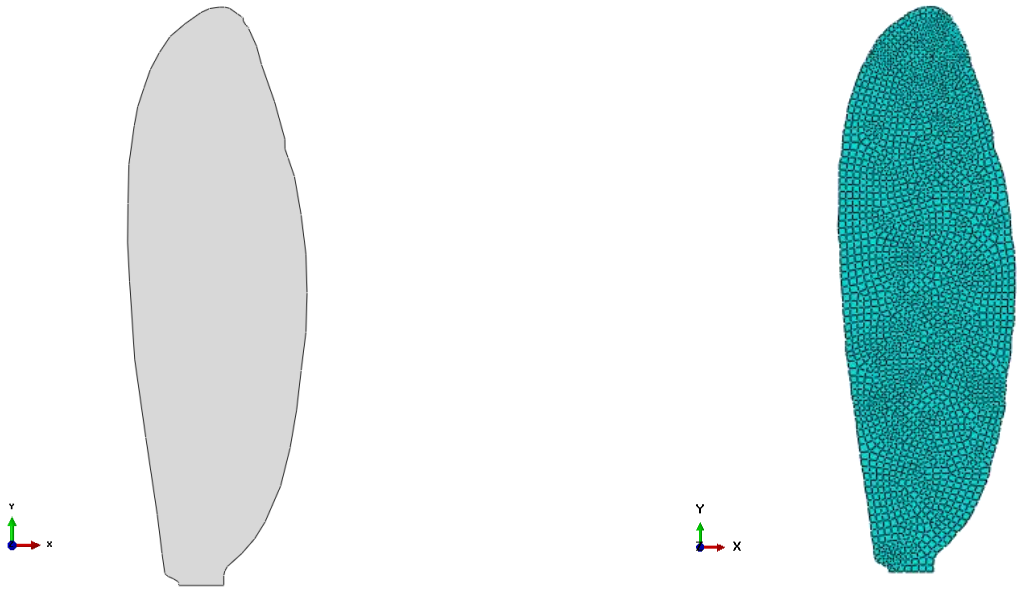

Figure 2.8. Membrane part (left) and membrane mesh (right)

On the other hand, the veins are modeled as 3-D wires with a tubular cross-sectional profile. The veins are meshed using B32 (3-node quadratic beam) type of element. A beam element is a one-dimensional line element in a 3-D space that has stiffness associated with deformation. These deformations consist of axial stretch, bending, or torsion. In other words,

these elements have six degrees of freedom. The vein pattern and its respective mesh are shown in Fig. 2.9.

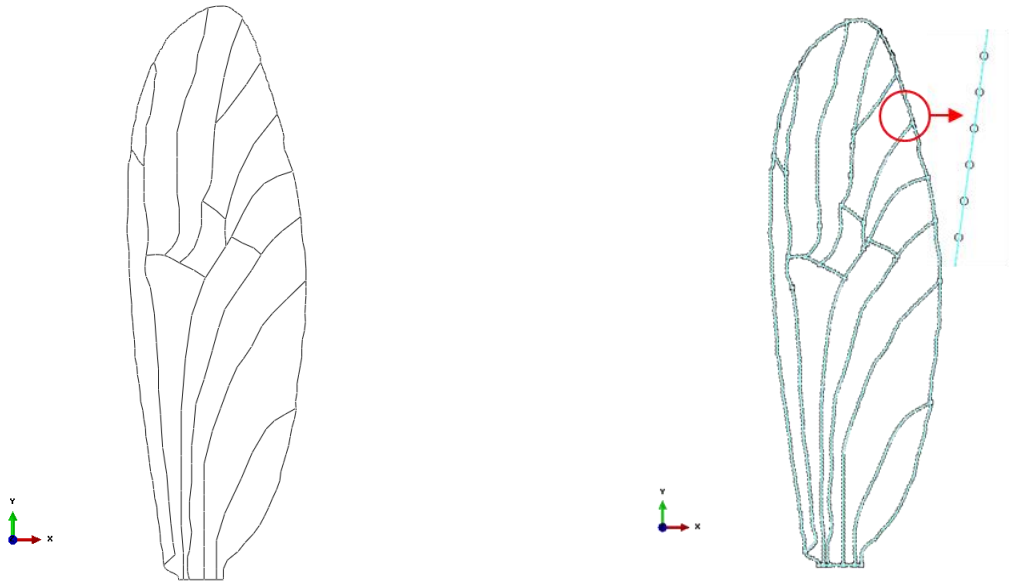

Figure 2.9. Vein pattern part (left) and vein mesh (right)

2.3.1.3. Materials Properties for the FE Model

Material properties for a crane fly (family *Tipulidae*) are required for the FE model. The material density of the wing cuticle is assigned to 1200 kg/m^3 as measured by Wainwright et al. [37] and used by Jongerius [24] and Ishihara [21]. A Poisson's ratio of 0.495 is used as measured in some biological materials by Wainwright et al. [37]. The effects of variation of Poisson's ratio can be considered negligible as investigated by Combes and Daniels [18]. Special care must be taken when assigning the Young's modulus. Recent studies reveal that the Young's modulus can vary widely within a wing as reported by Agrawal et al. [36], Combes and Daniels [20], and Smith et al. [38]. Unfortunately, accurate data regarding the variation of Young's modulus along the wing span of insects is still limited. However, to take into account the variation of stiffness along the spanwise *y*-direction of the wing, two sections of different vein diameters are identified through the micro-CT scan measurements and consequently

implemented into the FE model as done by Sims et al. [23]. For this FE model, the membrane and the veins are assigned a Young's modulus of 1.9 GPa and 4.0 GPa, respectively [23]. The material properties for the FE model are summarized in Table 2.5.

Table 2.5. Material properties for the FE model

Property	Membrane	Veins
Young's modulus (GPa)	1.9	4.0
Poisson's ratio	0.495	0.495
Density (kg/m^3)	1200	1200

2.3.1.4. Boundary Conditions and Constraints for the FE Model

For accurate physical behavior, the FE wing model must mimic the physical in-flight characteristics of a crane fly. Therefore, a clamped condition with all degrees of freedom fixed is assigned to the base of the wing to simulate the corresponding condition of a wing attached to the thorax of the insect. Similarly, a tie constraint is applied between the membrane and the veins so that they act as a single deformable body with the deformations coupled between each other.

2.3.2. Computational Fluid Dynamics Model

2.3.2.1. CFD Geometry Construction

An Abaqus/CFD model is developed to represent the surrounding air flowing over the wing. The CFD computational domain is modeled as a rectangular box that encloses a cavity with the exact dimensions of the forewing. The size of the CFD domain is chosen to be 30 mm height × 50 mm width × 70.0 mm length. With this dimensions the far-field boundaries are far enough not to affect the flow behavior in the vicinity to the forewing FE structure.

2.3.2.2. CFD Mesh Generation

The fluid domain is meshed using FC3D4 (4-node linear tetrahedral elements) type of element. The mesh is refined near the wing cavity to reduce the aspect ratio between the mesh of the CFD model and the mesh of the FE model. The respective fluid domain and its mesh are shown in Fig. 2.10. Furthermore, the mesh refinement is presented in Fig. 2.11.

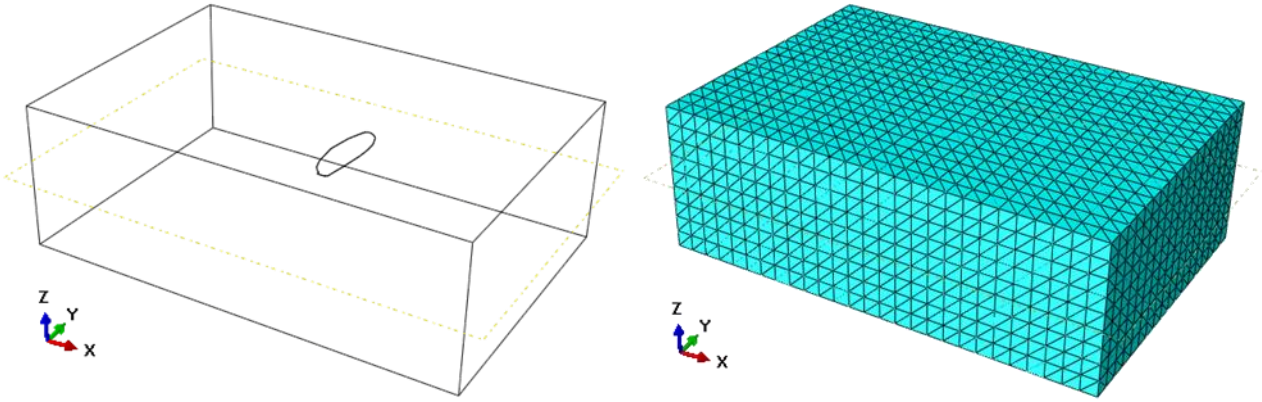

Figure 2.10. CFD domain (left) and CFD mesh (right)

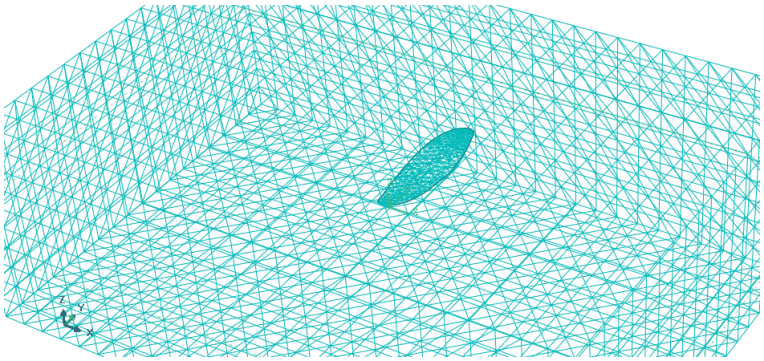

Figure 2.11. Mesh refinement near wing cavity

2.3.2.3. Materials Properties for the CFD Model

Air properties at standard atmospheric conditions are assigned to the CFD model. The fluid properties for the CFD model are summarized in Table 2.6.

Table 2.6. Fluid properties for the CFD model

Property	Value
Air density (kg/m^3)	1.225
Dynamic viscosity (kg/m·s)	1.983×10^{-5}

2.3.2.4. Boundary Conditions and Constraints for the CFD Model

The boundary conditions must not only mimic the low-speed flight conditions encountered by the crane fly but also satisfy the mathematical formulation of the CFD code. Therefore, to satisfy the first condition, an investigation of Reynolds number typically sustained by the crane fly is required. Recall that Reynolds number represents the ratio of inertial and viscous forces, and for the specific case of the crane fly it is mathematically defined by Eq. 2.1

$$\mathrm{Re} = \frac{\rho V_\infty c}{\mu} \tag{2.1}$$

During flapping flight, generation of wing circulation and vortex-based lift is enhanced due to the effect of viscous effects at low Reynolds number [4]. Estimates of Reynolds number for miniaturized insects range from 10 to 10^4 [4, 39–41]. For example, bumblebees and dragonflies operate at a Reynolds number around 4×10^3. At the lower end of the spectrum, fruit flies and chalcid wasps fly at Reynolds number of 200 and 20, respectively [42]. Therefore, boundary conditions are applied on the fluid domain for different freestream velocity magnitudes between the range of 10 mm/s to 1000 mm/s which corresponds to a Reynolds number of 2.7 and 270, respectively.

To satisfy the mathematical formulation of the CFD code, for steady and unsteady airflow, four boundary conditions are specified on the fluid domain: inlet, far-field, outlet, and symmetry. Similarly, two boundary conditions are assigned on the mesh: fixed and symmetry.

The boundary conditions for the CFD model are summarized in Table 2.7 and are described in terms of the coordinate system employed for the development of the computational model.

Table 2.7. Boundary conditions for the CFD model

Boundary condition	Parameter
Steady inlet velocity in *x*-, *y*-, and *z*-directions	$v_x = V_\infty \cos\theta$ mm/s; $v_y = 0$ mm/s; $v_z = V_\infty \sin\theta$ mm/s
Unsteady inlet velocity in *x*-, *y*-, and *z*-directions	$v_x = V_\infty \cos\theta + (V_\infty \cos\theta)\sin(\omega t)$ mm/s; $v_y = 0$ mm/s; $v_z = V_\infty \cos\theta + (V_\infty \cos\theta)\sin(\omega t)$ mm/s
Steady and unsteady outlet pressure	$p = 0$
Steady far-field velocity in *x*-, *y*-, and *z*-directions	$v_x = V_\infty \cos\theta$ mm/s; $v_y = 0$ mm/s; $v_z = V_\infty \sin\theta$ mm/s
Unsteady far-field velocity in *x*-, *y*-, and *z*-directions	$v_x = V_\infty \cos\theta + (V_\infty \cos\theta)\sin(\omega t)$ mm/s; $v_y = 0$ mm/s; $v_z = V_\infty \cos\theta + (V_\infty \cos\theta)\sin(\omega t)$ mm/s
Steady and unsteady symmetric velocity in *z*-direction	$v_z = 0$
Steady and unsteady mesh fixed deformation in *x*-, *y*-, and *z*-directions	$U_x = 0;\ U_y = 0;\ U_z = 0$
Steady and unsteady mesh symmetric deformation in *z*-direction	$U_z = 0$

2.3.3. Fluid-Structure Interaction

Fluid-structure interaction represents a class of multi-physics problem where fluid flow affects compliant structures, which in turn affects the fluid flow. Such behavior requires the

structural and fluid equations to be solved independently and interface loads and boundary conditions to be exchanged after a converged increment [35]. In this study, the Abaqus/CFD model consisting of the fluid domain is coupled with the Abaqus/Standard FE model consisting of the crane fly forewing through the co-simulation engine. Co-simulation interfaces across which data are exchanged during the co-simulation analysis are identified on each model. For the FE model, the fluid-structure interface is defined at the bottom surface of the wing. Similarly, for the CFD model, the fluid-structure interface is allocated to the extruded cavity inside the fluid domain. The co-simulation interfaces are presented in Fig. 2.12.

A frequency linear perturbation analysis step is selected to perform a modal analysis in vacuum. Lanczos eigensolver is selected to determine the first three natural frequencies and mode shapes of the FE model. For the FSI simulation, a dynamic-implicit step is selected in the FE model and an incompressible laminar flow analysis step is selected in the CFD model to determine the displacements of the wing under steady and unsteady airflows.

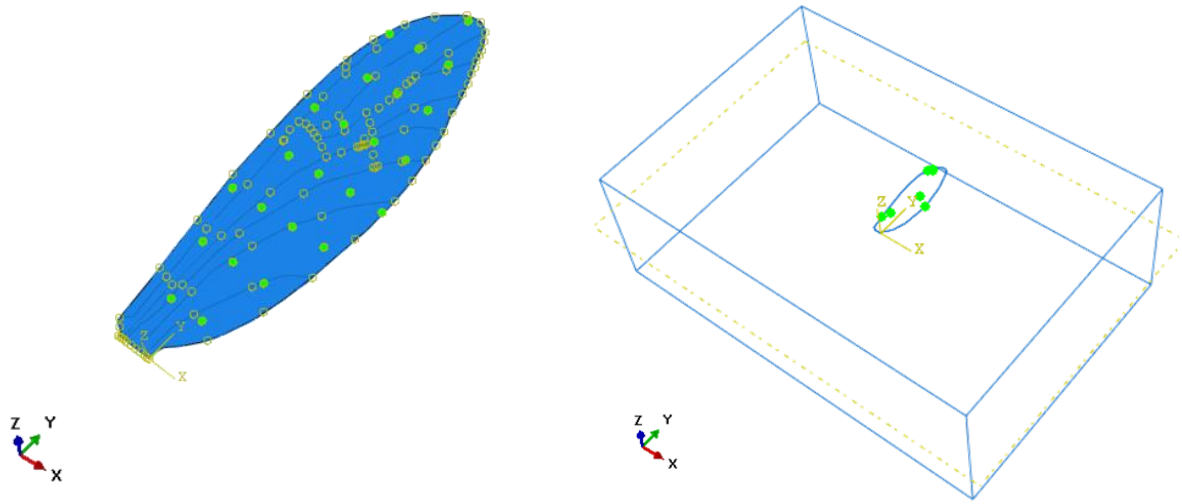

Figure 2.12. Co-simulation interfaces for the FE model (left) and for the CFD model (right)

CHAPTER 3. MATHEMATICAL MODELING

3.1. Vacuum Analysis Mathematical Formulation

The dynamics of a shell, which is a continuous elastic system, are mathematically modeled by partial differential equations derived from Newton's second law of motion.

3.1.1. Assumptions

The derivation of the equation of motion for the free vibration of a shell is based on the following assumptions:

1) The mass of the shell per unit area is constant; in other words, the shell is homogeneous.
2) The out of plane deflection *w(x, y, t)* of the shell is small compared to the size of the shell. Similarly, all angles of inclination are small.
3) Rotary inertia effects are neglected.

3.1.2. Governing Differential Equations

The governing differential equation for the free vibration of a shell is described in Eq. 3.1 [43].

$$D\nabla^4 w(x,y,t) + \rho h w_{tt}(x,y,t) = q \tag{3.1}$$

where

$$D = \frac{Eh^3}{12(1-\nu^2)} \tag{3.2}$$

3.1.3. Boundary and Initial Conditions

For the clamped condition at the bottom edge of the wing the deflection along that edge must be zero. Consider a domain Ω as shown in Fig. 3.1, if $\partial\Omega$ is the curve in the *xy* plane corresponding to the bottom edge of the membrane, the clamped boundary condition is mathematically defined in Eq. 3.3.

$$w(x, y, t) = 0 \quad for \quad x, y \in \partial\Omega \tag{3.3}$$

Similarly, the slope in the normal direction *n* to the boundary must be zero as shown in Eq. 3.4.

$$\frac{\partial w(x, y, t)}{\partial n} = 0 \quad for \quad x, y \in \partial\Omega \tag{3.4}$$

Furthermore, the initial conditions for this case are presented in Eqs. 3.5 and 3.6.

$$w(x, y, 0) = 0 \tag{3.5}$$

$$w_t(x, y, 0) = 0 \tag{3.6}$$

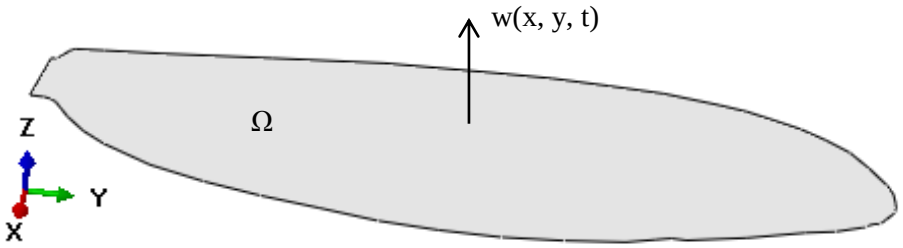

Figure 3.1. Domain for the mathematical formulation of the modal analysis of the crane fly forewing

3.2. Steady Flow over an Immersed Body Mathematical Formulation

This section presents the mathematical relationships that govern the steady fluid motion over an arbitrary body immersed on a fluid domain.

3.2.1. General Vector Form of Conservation Equations

The conservation of mass and momentum in their most general vector form are presented in Eqs. 3.7 and 3.8 [44].

Conservation of mass:

$$\frac{\partial \rho}{\partial t} + \vec{\nabla} \cdot (\rho \vec{V}) = 0 \tag{3.7}$$

Conservation of momentum:

$$\rho \frac{D\vec{V}}{Dt} = \rho \vec{g} - \vec{\nabla} p + \vec{\nabla} \tau'_{ij} \tag{3.8}$$

where

$$\tau'_{ij} = \mu \left(\frac{\partial V_i}{\partial x_j} + \frac{\partial V_j}{\partial x_i} \right) - \frac{2}{3} \mu \left(\vec{\nabla} \cdot \vec{V} \right) \lambda_{ij} \qquad \text{for} \qquad i, j, k = 1, 2, 3$$
$$\lambda_{ij} = \begin{cases} 0 & i \neq j \\ 1 & i = j \end{cases} \tag{3.9}$$

3.2.2. Assumptions

1) The system is at steady state meaning that there is no change with respect to time of any variable or property.
2) The flow is incompressible.
3) The flow is 2-D.
4) The flow is laminar with Reynolds number less than Reynolds critical number which is equal to 5×10^5.
5) The properties of the fluid remain constant across a small differential element.
6) Buoyancy terms are neglected.
7) The fluid is Newtonian meaning that there is linear relationship between shear and strain.

3.2.3. Governing Differential Equations

Considering the assumptions stated previously, the conservation equations are expanded from the general vector form and are presented in Cartesian coordinates in Eqs. 3.10–3.12 [44].

Conservation of mass:

$$\frac{\partial v_x}{\partial x} + \frac{\partial v_y}{\partial y} = 0 \tag{3.10}$$

Conservation of momentum:
x-direction:

$$v_x \frac{\partial v_x}{\partial x} + v_y \frac{\partial v_x}{\partial y} = -\frac{1}{\rho}\frac{\partial p}{\partial x} + \upsilon\left(\frac{\partial^2 v_x}{\partial x^2} + \frac{\partial^2 v_x}{\partial y^2}\right) \tag{3.11}$$

y-direction:

$$v_x \frac{\partial v_y}{\partial x} + v_y \frac{\partial v_y}{\partial y} = -\frac{1}{\rho}\frac{\partial p}{\partial y} + \upsilon\left(\frac{\partial^2 v_y}{\partial x^2} + \frac{\partial^2 v_y}{\partial y^2}\right) \tag{3.12}$$

3.2.4. Boundary Conditions

Equations 3.10–3.12 are non-linear partial differential equations that require the specification of Neumann, Dirichlet, or mixed type of boundary conditions at the surface of the immersed body and at different location of the fluid domain.

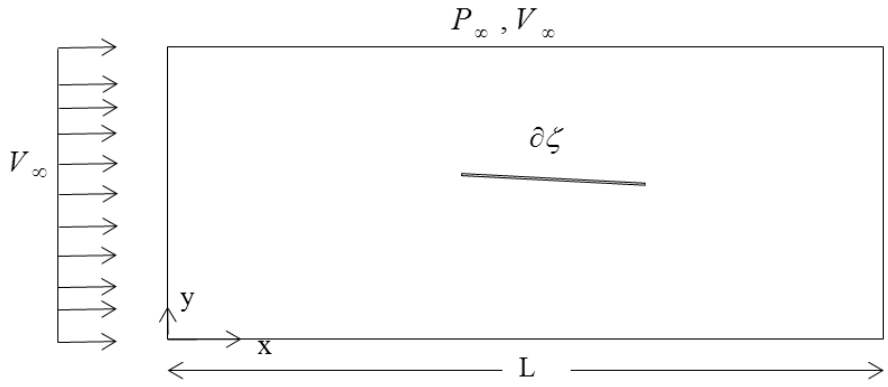

Figure 3.2. Schematic for mathematical formulation of steady flow over an immersed body

For the problem to be well posed, the following boundary conditions are required to solve Eqs. 3.10–3.12:

- 2 boundary conditions on v_x in *x*-direction
- 2 boundary conditions on v_x in *y*-direction
- 2 boundary conditions on v_y in *x*-direction

- 2 boundary conditions on v_y in *y*-direction
- 1 boundary condition on p in *x*-direction
- 1 boundary condition on p in *y*-direction

The boundary conditions at the solid surface of the immersed body refer to the no-slip condition which states that the fluid must stick to the surface of the immersed body due to viscous effects. Referring to Fig. 3.2 and considering the surface of the solid object as $\partial\zeta(x, y)$, these boundary conditions are expressed mathematically in Eqs. 3.13 and 3.14.

$$v_x = 0 \quad at \quad x, y \in \partial\zeta \tag{3.13}$$

$$v_y = 0 \quad at \quad x, y \in \partial\zeta \tag{3.14}$$

The boundary conditions at the far field state that the velocity must be equal to the freestream velocity given that the flow in this region is not affected by the interaction with the immersed body. Mathematically, these boundary conditions are show in Eqs. 3.15 and 3.16.

$$\begin{gathered} v_x = V_\infty \quad at \quad y \to \infty \quad for \quad 0 \le x < L \\ or \\ \frac{\partial v_x}{\partial y} = 0 \quad at \quad y \to \infty \quad for \quad 0 \le x < L \end{gathered} \tag{3.15}$$

$$v_y = 0 \quad at \quad y \to \infty \quad for \quad 0 \le x < L \tag{3.16}$$

The boundary conditions at the entrance or inlet of the computational domain state the velocity must be equal to the freestream velocity. Mathematically, these boundary conditions are show in Eqs. 3.17 and 3.18.

$$v_x = V_\infty \quad at \quad x = 0 \quad for \quad 0 \le y < \infty \tag{3.17}$$

$$v_y = 0 \quad at \quad x = 0 \quad for \quad 0 \le y < \infty \tag{3.18}$$

Lastly, pressure boundary conditions are prescribed on the domain. Mathematically, they are expressed in Eqs. 3.19 and 3.20.

$$P = P_\infty \quad at \quad x = L \quad for \quad 0 \le y < \infty \tag{3.19}$$

$$P = P_\infty \quad at \quad y \to \infty \quad for \quad 0 \le x < L \tag{3.20}$$

3.3. Unsteady Flow over an Immersed Body Mathematical Formulation

This section presents the mathematical relationships that govern the unsteady fluid motion over an arbitrary body immersed on a fluid domain.

3.3.1. Governing Differential Equations

The conservation of mass and momentum in their most general vector form are presented in Eqs. 3.21 and 3.22.

Conservation of mass:

$$\frac{\partial \rho}{\partial t} + \vec{\nabla} \cdot (\rho \vec{V}) = 0 \tag{3.21}$$

Conservation of momentum:

$$\rho \frac{D\vec{V}}{Dt} = \rho \vec{g} - \vec{\nabla} p + \vec{\nabla} \tau'_{ij} \tag{3.22}$$

where

$$\tau'_{ij} = \mu \left(\frac{\partial V_i}{\partial x_j} + \frac{\partial V_j}{\partial x_i} \right) - \frac{2}{3} \mu \left(\vec{\nabla} \cdot \vec{V} \right) \lambda_{ij} \qquad \text{for} \qquad i, j, k = 1, 2, 3$$
$$\lambda_{ij} = \begin{cases} 0 & i \neq j \\ 1 & i = j \end{cases} \tag{3.23}$$

3.3.2. Assumptions

1) The flow is incompressible.
2) The flow is 2-D.
3) The flow is laminar with Reynolds number less than Reynolds critical number which is equal to 5×10^5.
4) The properties of the fluid remain constant across a small differential element.
5) Buoyancy terms are neglected.
6) The fluid is Newtonian meaning that there is linear relationship between shear and strain.

3.3.3. Governing Differential Equations

Considering the assumptions stated previously, the conservation equations are expanded from the general vector form and are presented in Cartesian coordinates in Eqs. 3.24–3.26 [44].

Conservation of ass:

$$\frac{\partial \rho}{\partial t}+\frac{\partial v_x}{\partial x}+\frac{\partial v_y}{\partial y}=0 \tag{3.24}$$

Conservation of momentum:
x-direction:

$$\frac{\partial v_x}{\partial t}+v_x\frac{\partial v_x}{\partial x}+v_y\frac{\partial v_x}{\partial y}=-\frac{1}{\rho}\frac{\partial p}{\partial x}+\upsilon\left(\frac{\partial^2 v_x}{\partial x^2}+\frac{\partial^2 v_x}{\partial y^2}\right) \tag{3.25}$$

y-direction:

$$\frac{\partial v_y}{\partial t}+v_x\frac{\partial v_y}{\partial x}+v_y\frac{\partial v_y}{\partial y}=-\frac{1}{\rho}\frac{\partial p}{\partial y}+\upsilon\left(\frac{\partial^2 v_y}{\partial x^2}+\frac{\partial^2 v_y}{\partial y^2}\right) \tag{3.26}$$

3.3.4. Boundary Conditions

Equations 3.24–3.26 are non-linear partial differential equations that require the specification of Neumann, Dirichlet, or mixed type of boundary conditions at the surface of the immersed body and at different location of the fluid domain.

For the problem to be well posed, the following boundary conditions are required to solve Eqs. 3.24–3.26:

- 2 boundary conditions on v_x in *x*-direction
- 2 boundary conditions on v_x in *y*-direction
- 2 boundary conditions on v_y in *x*-direction
- 2 boundary conditions on v_y in *y*-direction
- 1 boundary condition on p in *x*-direction
- 1 boundary condition on p in *y*-direction
- Initial conditions on v_x and v_y

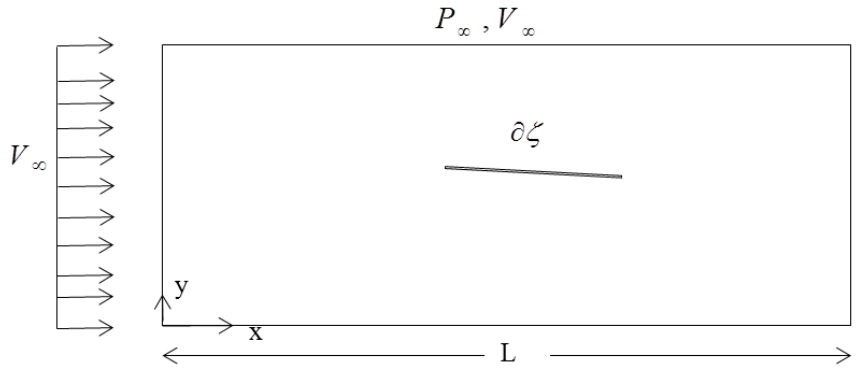

Figure 3.3. Schematic for mathematical formulation of unsteady flow over an immersed body

The boundary condition at the solid surface of the immersed body refer to the no-slip condition which states that the fluid must stick to the surface of the immersed body due to viscous effects. Referring to Fig. 3.3 and considering the surface of the solid object as $\partial\zeta(x, y)$, these boundary conditions are expressed mathematically in Eqs. 3.27 and 3.28.

$$v_x = 0 \quad at \quad x, y \in \partial\zeta \quad \text{for} \quad t \geq 0 \tag{3.27}$$

$$v_y = 0 \quad at \quad x, y \in \partial\zeta \quad \text{for} \quad t \geq 0 \tag{3.28}$$

The boundary conditions at the far field state that the velocity must be equal to the freestream velocity given that the flow in this region is not affected by the interaction with the immersed body. Mathematically, these boundary conditions are show in Eqs. 3.29 and 3.30.

$$\begin{gathered} v_x = V_\infty \sin(\omega t) \quad at \quad y \to \infty \quad for \quad 0 \leq x < L, \;\; t \geq 0 \\ or \\ \frac{\partial v_x}{\partial y} = 0 \quad at \quad y \to \infty \quad for \quad 0 \leq x < L, \;\; t \geq 0 \end{gathered} \tag{3.29}$$

$$v_y = 0 \quad at \quad y \to \infty \quad for \quad 0 \leq x < L, \;\; t \geq 0 \tag{3.30}$$

The boundary conditions at the entrance or inlet of the computational domain states the velocity must be equal to the freestream velocity. Mathematically, these boundary conditions are show in Eqs. 3.31 and 3.32.

$$v_x = V_\infty \quad at \quad x = 0 \quad for \quad 0 \leq y < \infty \tag{3.31}$$

$$v_y = 0 \quad at \quad x = 0 \quad for \quad 0 \leq y < \infty \tag{3.32}$$

Lastly, pressure boundary conditions are prescribed on the domain. Mathematically, they are expressed in Eqs. 3.33 and 3.34.

$$P = P_{\infty} \quad at \quad x = L \quad for \quad 0 \le y < \infty \tag{3.33}$$

$$P = P_{\infty} \quad at \quad y \to \infty \quad for \quad 0 \le x < L \tag{3.34}$$

The initial condition is required for this formulation is shown in Eqs. 3.35 and 3.36.

$$v_x = o \quad for \quad t = 0 \tag{3.35}$$

$$v_y = o \quad for \quad t = 0 \tag{3.36}$$

CHAPTER 4. RESULTS AND DICUSSIONS

4.1. Vacuum Analysis

4.1.1. FE Model Validation

To validate the FE model, the natural frequencies of a FE model of an elliptical membrane in vacuum are calculated and compared with those from the analytical solution from Mathieu functions [45]. The FE elliptical membrane model is developed considering a thickness of 0.016 mm and major and minor radii of 6.93 mm and 1.6 mm, respectively; which fairly agrees with the corresponding dimensions of a crane fly forewing. Material properties of the veins are assigned to the FE model.

Table 4.1. Comparison between the natural frequencies of the FE elliptical model and the analytical solution in vacuum

Mode	Natural frequency analytical solution (Hz)	FE model case 1 (number of nodes: 673)		FE model case 2 (number of nodes: 1200)	
		Natural frequency (Hz)	Percent error (%)	Natural frequency (Hz)	Percent error (%)
First mode	163.55	163.55	0.00	163.55	0.00
Second mode	186.26	186.28	0.01	186.26	0.00
Third mode	210.22	210.24	0.02	210.22	0.03

The variation of the natural frequencies of the FE elliptical model and the analytical solution is less than 1.0% as shown in Table 4.1. For a total of 673 nodes with 3658 degrees of freedom, the first three natural frequencies of the FE elliptical model are 163.55, 186.28, and 210.24 Hz, respectively. These numbers are in excellent agreement with the first three natural frequencies of 163.55, 186.26, and 210.22 Hz, respectively, from the analytical solution of the elliptical membrane. Most importantly, the aforementioned results provide a level of confidence for the vacuum analysis conducted in this study.

4.1.2. Mesh Independence Study for the Vacuum Analysis

The variation of the natural frequencies of the crane fly forewing in vacuum with respect to the mesh is studied and presented in Fig. 4.1. Results indicate that the natural frequencies are mesh independent for mesh grids with 1000 nodes or higher. The mesh is sufficiently refined at this point since further variation of element size produces a negligible change in the calculation of the natural frequencies.

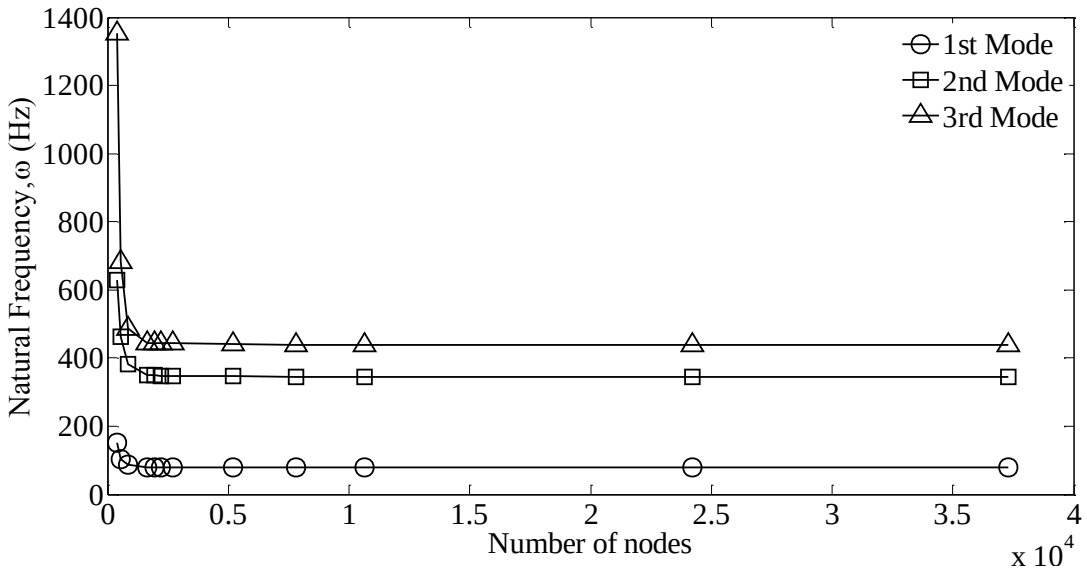

Figure 4.1. Variation of the natural frequencies of the crane fly forewing in vacuum with respect to the number of nodes of the FE model

4.1.3. Natural Frequencies and Mode Shapes of Crane Fly Forewing in Vacuum

The first four natural frequencies of the crane fly forewing in vacuum are computed at 2695 nodes (12,802 degrees of freedom). Natural frequency of the forewing increases with mode as shown in Table 4.2. The natural frequency of the first mode is approximately 4 times less, 5 times less, and 13 times less than those from the second, third, and fourth modes, respectively. This behavior suggests that the first four natural frequencies dominate the vibration response; therefore, they are sufficient for the purpose of this analysis. Furthermore, these results reiterate

that the crane fly is unlikely to reach its natural frequency and resonate during flight since previous studies indicate that the crane fly flaps its wing at values near 45.5 Hz [17, 21].

Table 4.2. Natural frequencies of the crane fly forewing in vacuum

Mode	Natural frequency (Hz)
First mode	79.97
Second mode	347.89
Third mode	442.54
Fourth mode	1042.9

The first four mode shapes are depicted in Fig. 4.2. The first mode shape shows the location of the maximum displacement at the tip of the wing and a bending deformation response that resembles that of a cantilever beam. This behavior is expected given the inherent stiffness variation along the spanwise *y*-direction of the wing implemented in the FE model. The second mode shape shows the location of maximum deformation at the middle section of the leading and trailing edge of the wing with a torsional deformation along a nodal line in the spanwise *y*-direction. This structural response identifies local regions at the leading and trailing edge as possible locations where the insect wing is less rigid. The third mode shape displays the maximum deformation at the tip of the wing with a bending deformation response similar to a cantilever beam with two opposite point loads. Furthermore, the latter mode presents two nodal lines, one developed near the root of the wing, and the second one developed near the center of the spanwise *y*-direction, both extending completely along the chordwise *x*-direction. Lastly, the fourth mode shape presents two similar nodal lines with respect to the third mode; however, a localized region of high deformation is developed at the bottom section of the trailing edge.

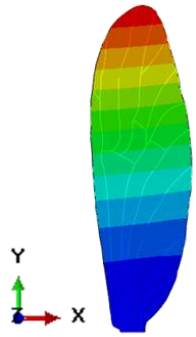

a. Front view of the first mode shape

b. Side view of the first mode shape

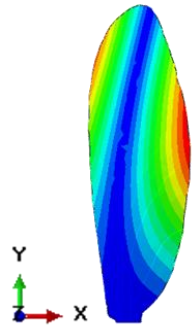

a. Front view of the second mode shape

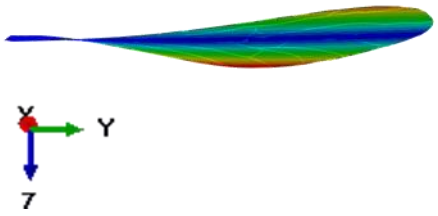

b. Side view of the second mode shape

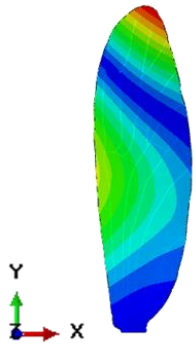

a. Front view of the third mode shape

b. Side view of the third mode shape

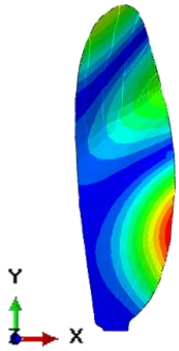

a. Front view of the fourth mode shape

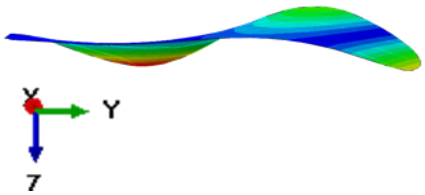

b. Side view of the fourth mode shape

Figure 4.2. First (at 79.97 Hz), second (at 347.89 Hz), third (at 442.54 Hz), and fourth mode shape (at 1042.9 Hz) of the crane fly forewing in vacuum

4.2. Steady Airflow Fluid-Structure Interaction Analysis

4.2.1. CFD Model Validation

To validate the CFD model, a benchmark case of the boundary layer development for steady incompressible flow over a flat plate is investigated and compared with that from the analytical solution from Blasius [44]. The boundary layer thickness is defined as the locus points where the velocity parallel to the plate reaches 99 percent of the freestream velocity. Mathematically, it is defined in Eq. 4.1,

$$\delta_x \approx \frac{5x}{\mathrm{Re}_x^{1/2}} \approx \frac{5x}{\sqrt{\frac{\rho V_\infty x}{\mu}}} \approx 5\sqrt{\frac{\mu x}{\rho V_\infty}} \tag{4.1}$$

A CFD model is developed and sized based on a Reynolds number of 270 and freestream velocity of 1 m/s, which are conditions typically encountered in insect flight. The results of this model and the analytical solution are presented qualitatively in Fig. 4.3 and numerically in Table 4.3. The profile for the *x*-component of velocity predicted by the numerical solution fairly agrees with the analytical solution from Blasius theory. It is anticipated that the velocity at the wall of the flat plate is zero due to the no slip condition with a nonlinear increment until it reaches the freestream velocity as seen in Fig. 4.3. Furthermore, as presented in Table 4.3, a fair agreement, with percent errors less than 18 %, is found between the two solutions when calculating and comparing the boundary layer thickness at different location. Both solutions accurately predict that the boundary layer thickness increases along the length of the flat plate. From this analysis, the implementation of a CFD model for external flow over an object is feasible.

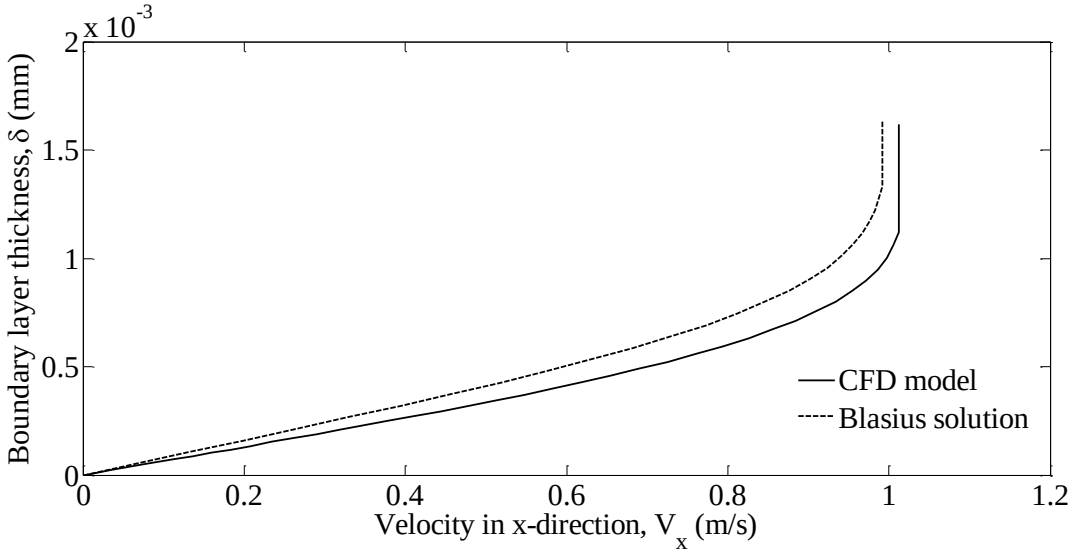

Figure 4.3. Comparison between the CFD model solution and the Blasius solution for V_x velocity profile along the trailing edge of the flat plate

Table 4.3. Comparison between the boundary layer of the CFD model solution and the Blasius solution

Location along flat plate (m)	**Boundary layer thickness Blasius solution, δ (m)**	**Boundary layer thickness FSI solution (m) δ**	**Percent error (%)**
0.2L	5.9472×10^{-4}	6.3423×10^{-4}	6.64
0.5L	9.4034×10^{-4}	7.8580×10^{-4}	16.43
L	1.3298×10^{-3}	1.1003×10^{-3}	17.26

4.2.2. Mesh Independence Study for the FSI Simulation

The mesh independence of the results from the FSI simulation is investigated by considering a case with steady airflow and a freestream velocity of 10 mm/s. For this study, the convergences of the results for both models are monitored by performing different simulations in which the number of nodes of one model is varied while the number of nodes of the other model is kept constant. For an easier comparison of results, a specific node is monitored in the FE model and referred as “node A” as shown in Fig. 4.4. On the other hand, for the CFD model the total lift force on the wing surface is examined.

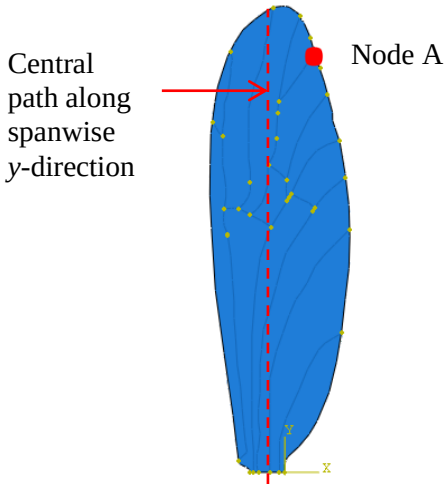

Figure 4.4. Location of node A (0.899 mm, 12.543 mm) and central path along spanwise *y*-direction for monitoring of convergence and analysis of results, respectively

The variation of the deformation of node A with respect to a change in the mesh of the FE model only is investigated and presented in Fig.4.5. For an accurate coupling of the co-simulation boundaries, the FE model requires a more refined mesh than the vacuum analysis. The results suggest that the calculations from the FSI simulations are mesh independent for discretized grids in the FE model with approximately 8000 nodes or higher.

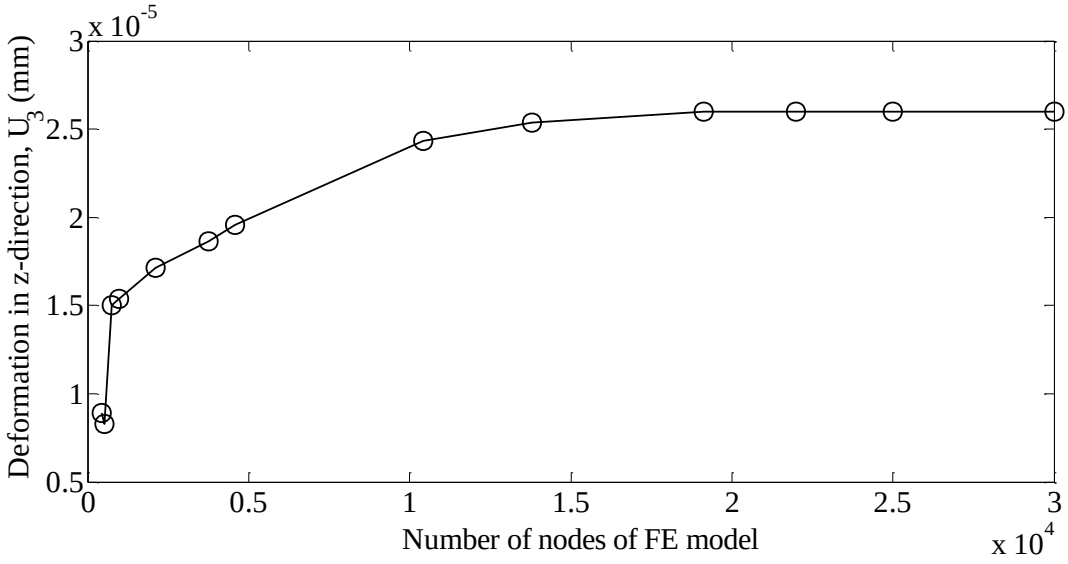

Figure 4.5. Mesh independence study for the FSI simulation done by monitoring the variation of the deformation of node A with respect to a change of the number of nodes in the FE mesh only

A similar mesh independence study is conducted for the CFD model. The variation of the resultant lift force on the FSI surface with respect to a change in the mesh of the CFD model is investigated and presented in Fig. 4.6. The results indicate that the calculations from the FSI simulations are mesh independent discretized grids in the CFD model with approximately 50,000 nodes or higher. Therefore, both mesh independence studies suggest an FSI simulation composed of an FE model with 8000 nodes or higher and a CFD model with 50,000 nodes or higher.

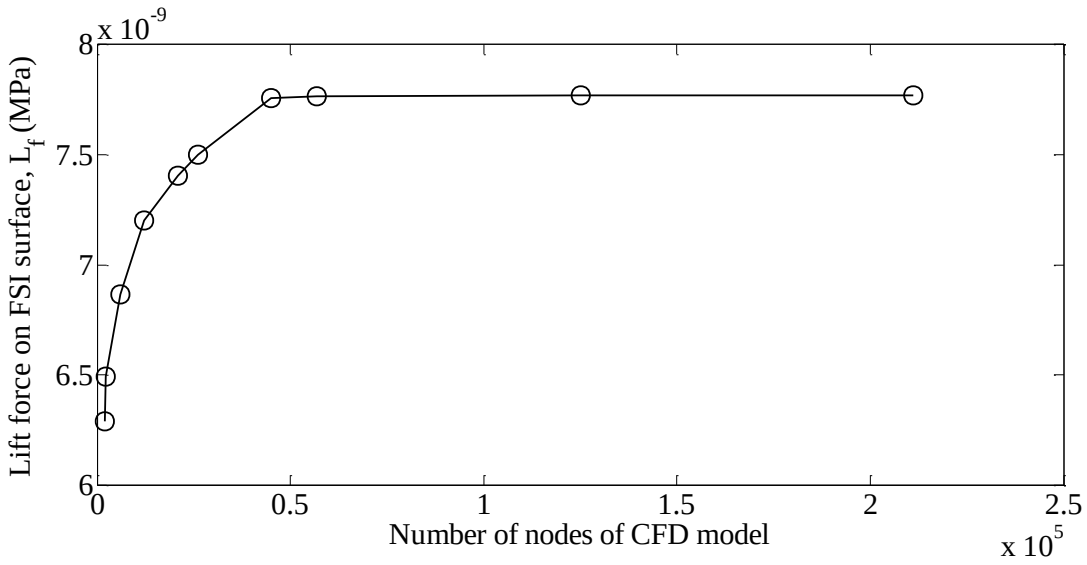

Figure 4.6. Mesh independence study for the FSI simulation done by monitoring the variation of the total lift force on the FSI surface with respect to a change of the number of nodes in the CFD mesh only

4.2.3. Structural Dynamic Response of Crane Fly Forewing under Steady Airflow

The deformations of the crane fly forewing under steady airflow at different freestream velocities are calculated from the FSI simulations and are shown in Fig. 4.7. The freestream velocities considered represent the ranges of Reynolds number at which the crane fly typically hovers. In general, the deformation and stress distributions are similar for all cases; however, the magnitudes are different. Furthermore, the *z*-component of deformation or out-of-plane deformation is dominant and increases nonlinearly with freestream velocity and along the

spanwise *y*-direction as shown in Fig. 4.8. It is noticeable that the deformation at the base of the wing and its surroundings is almost negligible due to the clamped condition assigned to the FE model and the stiffness provided in that area by the thicker vein pattern. Contrarily, the maximum deformation is estimated near the tip of the wing where the stiffness is significantly less compared to the corresponding one at the root of the wing, mainly due to the presence of thin structural veins. This nonuniform deformation provides a passive mechanism of adjusting the camber of the wing during hovering flight. Furthermore, the results from the stress analysis reveal higher concentration of stress at the root of the wing while the tip presents almost nothing. This behavior is expected as most of the stiffness of the wing is allocated to this region where the main veins are located and where the wing is attached to the thorax of the insect. In real life, this stress would be absorbed by the muscles located at the root of the wing that provide the required flapping motion. Lastly, the aerodynamic efficiency of the crane fly forewing is investigated by calculating the coefficients of lift and drag shown in Fig. 4.9. As expected, higher freestream velocities generate higher magnitudes of lift at an expense of an increase of drag. However, at low freestream velocities, the crane fly forewing still shows to be aerodynamically efficient with ratios of C_L/C_D greater than unity meaning that the lift forces exceed the drag generation.

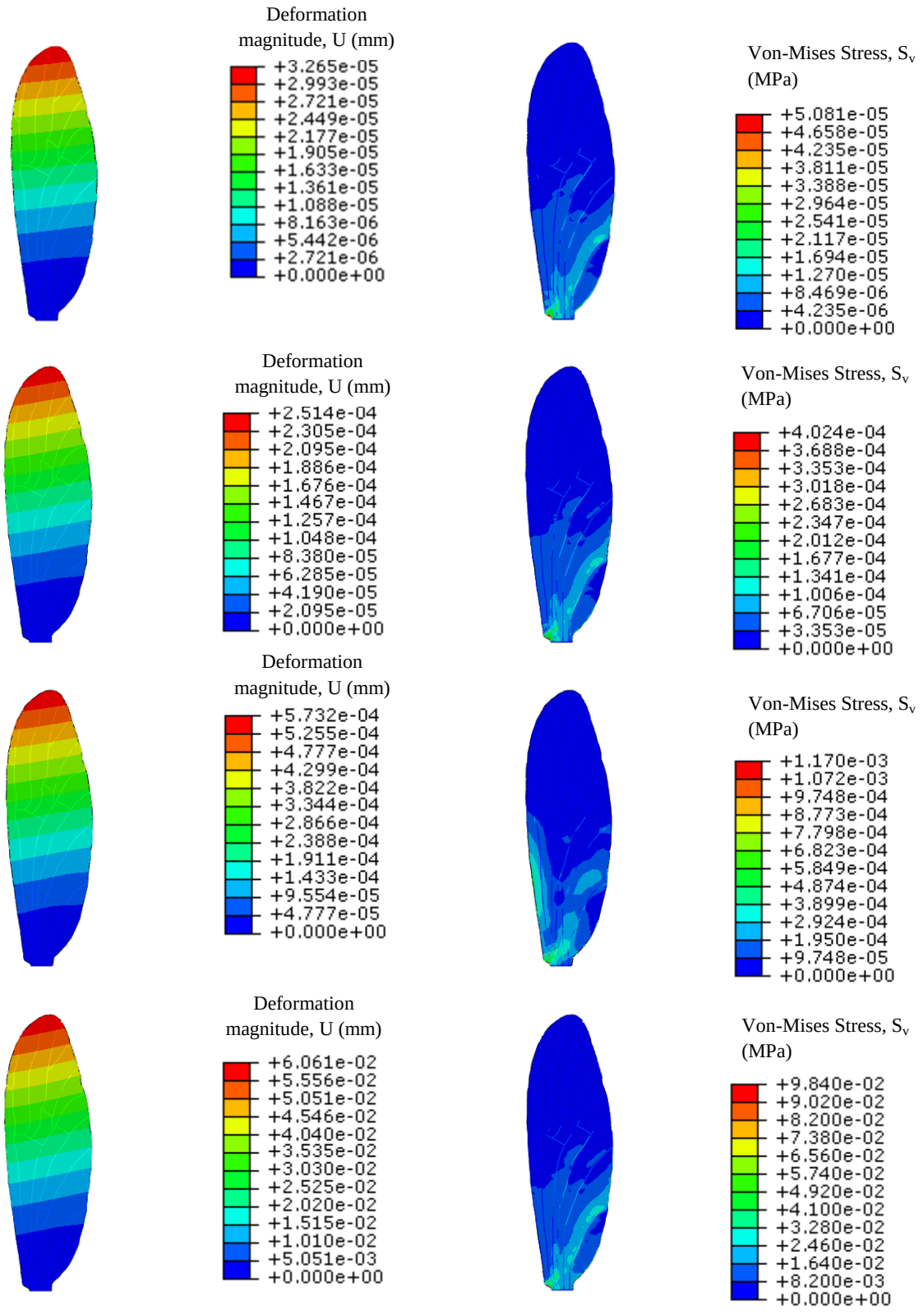

Figure 4.7. Deformation (left) and Von-Mises stress (right) of the crane fly forewing under steady airflow at 10 mm/s (first row), 50 mm/s (second row), 100 mm/s (third row), and 1000 mm/s (fourth row)

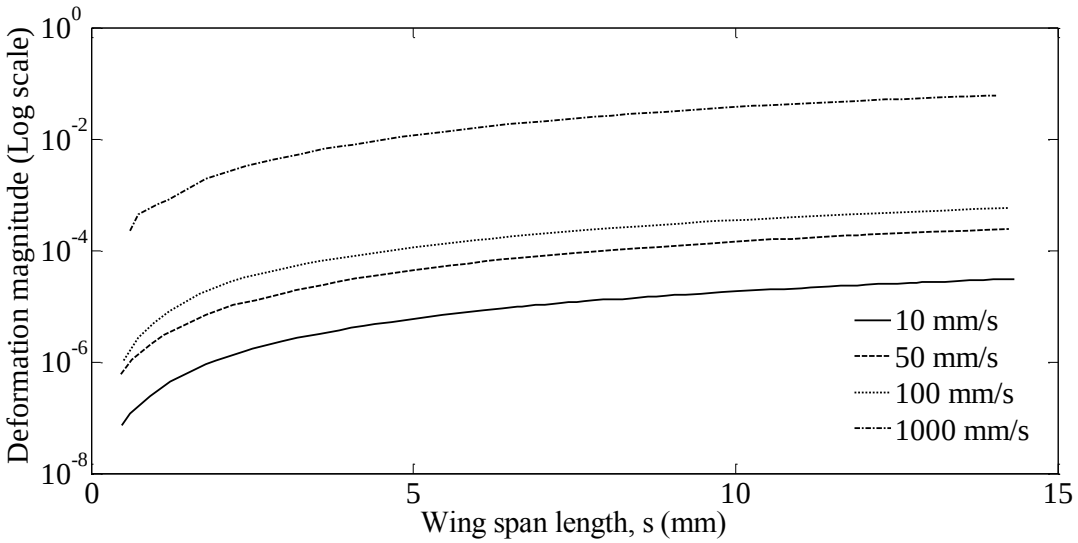

Figure 4.8. Deformation magnitude along a central path in the spanwise *y*-direction for steady airflow at different freestream velocities

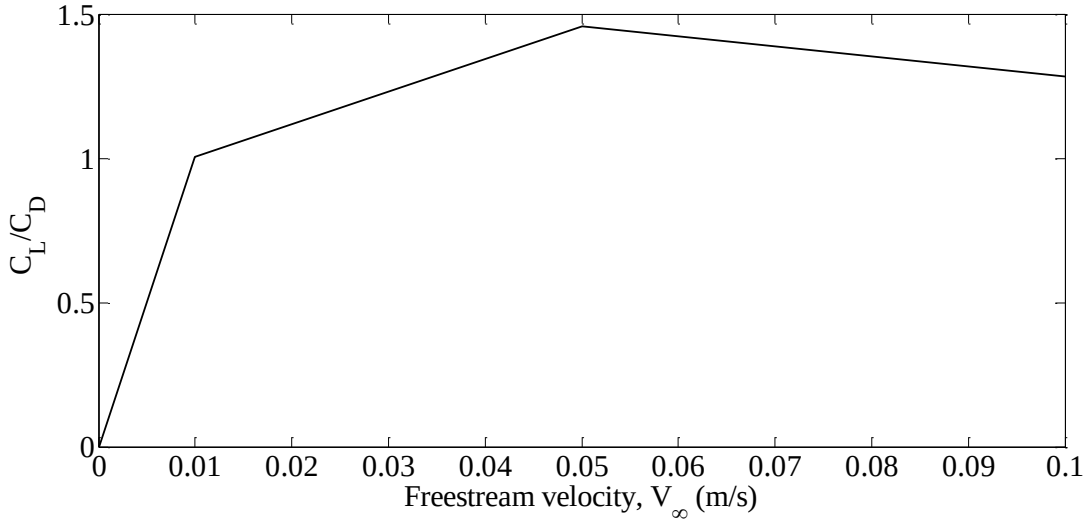

Figure 4.9. Aerodynamic efficiency of the crane fly forewing at different freestream velocities

4.2.4. Analysis of the Deformation Response for Steady Airflow at 1000 mm/s Freestream Velocity

The case for a freestream velocity of 1000 mm/s is selected for a detailed analysis since it corresponds to the upper limit of operating Re of the crane fly and a more typical environmental condition. Overall, the deformation response can be accurately described by monitoring the

deformation magnitudes along a central path in the spanwise *y*-direction which originates from the center of the root of the wing as shown in Fig. 4.10. The aforementioned plot accurately describes a negligible deformation at the root of the wing and a nonlinear increase of deformation along the spanwise *y*-direction.

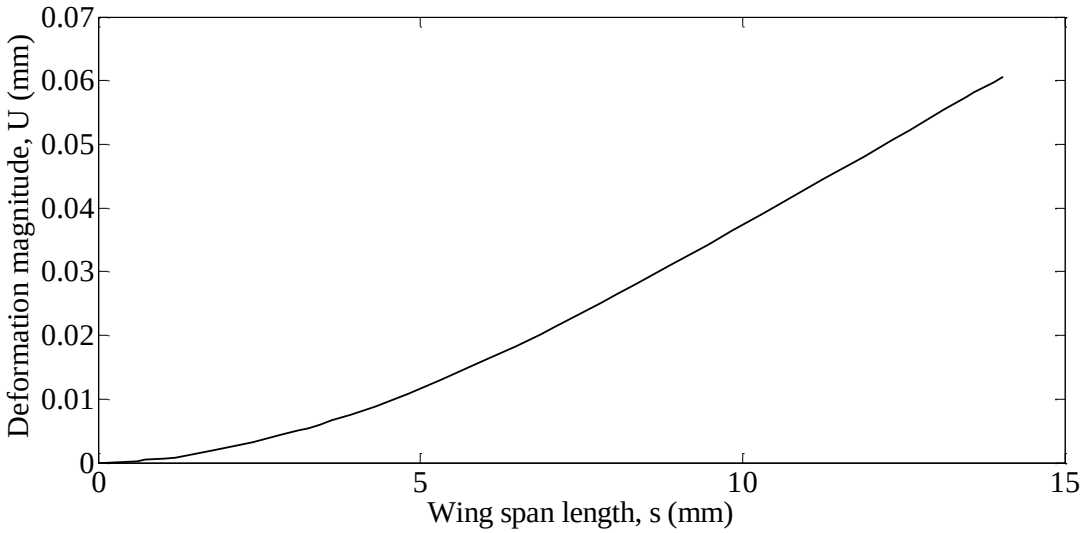

Figure 4.10. Deformation magnitude along a central path in the spanwise *y*-direction for steady airflow at a freestream velocity of 1000 mm/s

Nevertheless, analyzing the displacements components separately provides an insight of the flexible regions on the wing. Figure 4.11 shows the displacement contours U_x, U_y, and U_z which represents the displacements components in the *x*-, *y*-, *z*- direction, respectively. It is noticeable that the *z*-displacement or out-of-plane displacement dominates the deformation response with higher deformation magnitudes with respect to the others. Furthermore, the contour for the *y*-displacement shows maximum and minimum displacements at the trailing and leading edge, revealing regions of relative flexibility. More importantly, this behavior suggests that the wing is able to twist, which has been identified previously as an important feature that generates lift. Lastly, the *x*-displacement shows a deformation distribution similar to the one

from the *z*-displacement component with higher deformation at the tip of the wing where the stiffness of the structure is significantly lower.

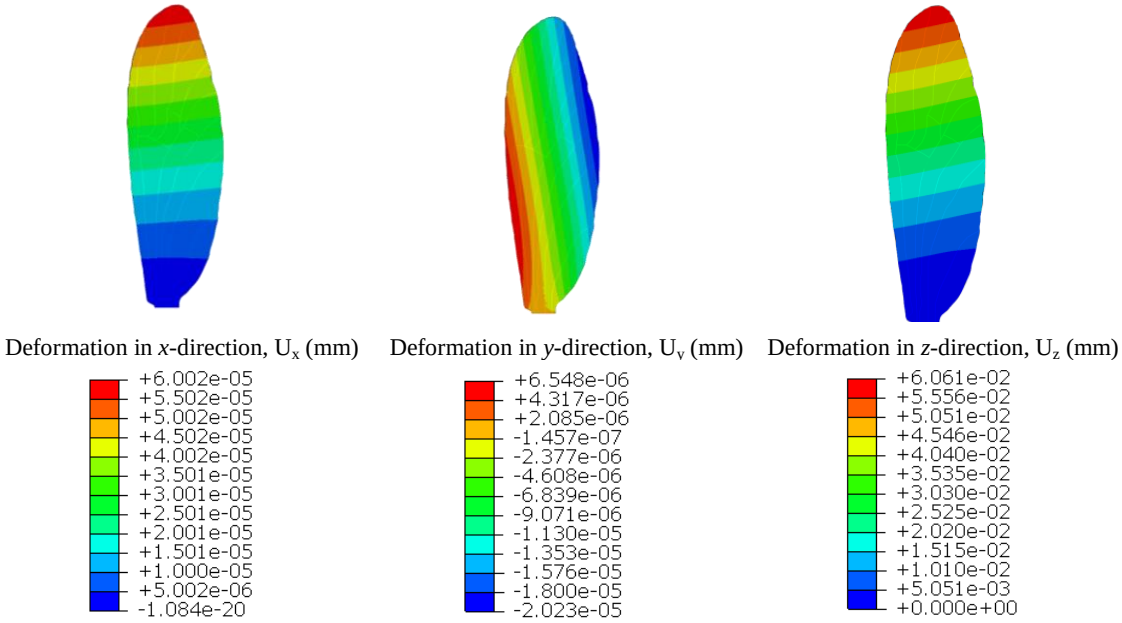

Figure 4.11. U_x (left), U_y (center), and U_z (right) components of displacement for steady airflow at a freestream velocity of 1000 mm/s

4.3. Unsteady Airflow Fluid-Structure Interaction Analysis

4.3.1. Deformation of Crane Fly Forewing under Unsteady Airflow

The deformations of the crane fly forewing under unsteady airflow are shown in Fig. 4.13. The deformation in the *z*-direction is chosen for representation since the out-of-plane deformation dominates the overall response of the structure. The periodic nature of the sinusoidal amplitude is reflected on the structural dynamic response of the crane fly forewing as it can be seen through the contours of the deformations at three different time frames, e.g. 0.25 s, 0.50 s, and 0.75 s which corresponds to the maximum, steady, and minimum deformation experienced by the forewing, respectively. In general, the deformation response is almost identical to the

corresponding one in steady state, with the deformation increasing nonlinearly from the root of the wing to its tip; however, with periodic changes in amplitude.

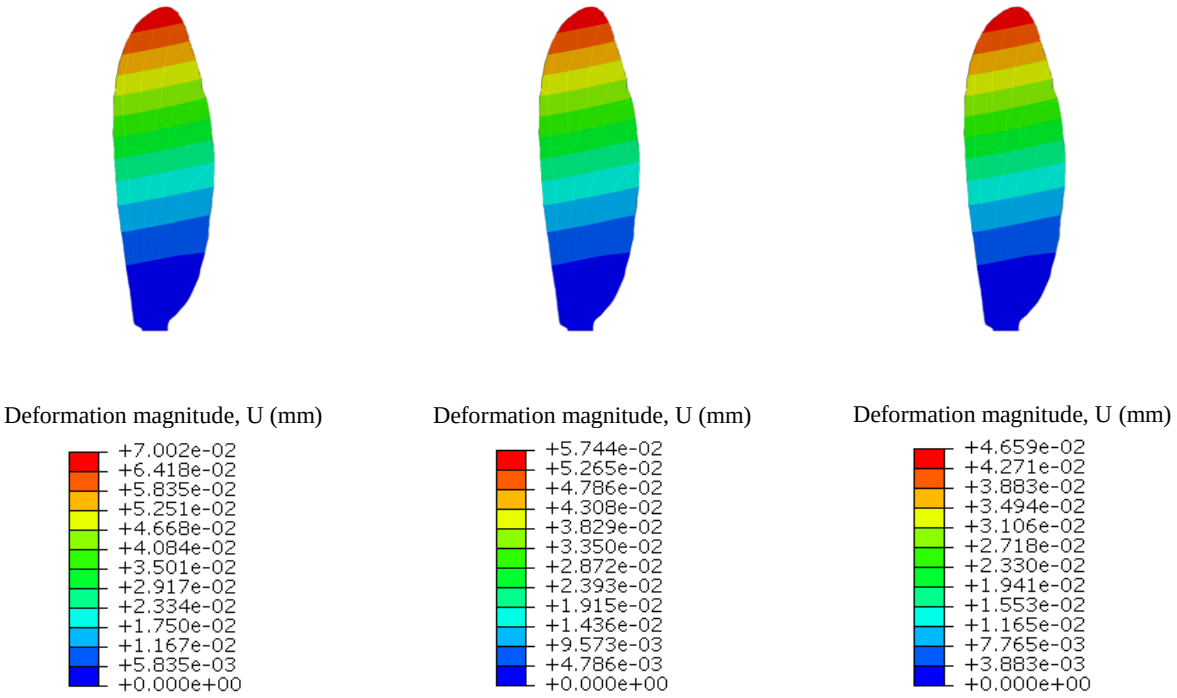

Figure 4.12. Deformation of the crane fly forewing under unsteady airflow at 0.25 s (left), 0.50 s (center), and 0.75 s (right) for a freestream velocity of 1000 mm/s

CHAPTER 5. CONCLUSIONS

The remarkable maneuverability and aerodynamic efficiency of insects have created an intrinsic interest on learning the mechanisms that govern insect flight and consequently consider their further application in engineered devices, namely micro air vehicles. However, in order to implement such mechanisms into these devices, the wings from micro air vehicles must be optimized, aerodynamically efficient structures. Therefore, a qualitative and quantitative analysis of the structural properties and dynamic response of insect wings is seen as the key element for a successful biomimic implementation. The aforementioned application is the motivation of this study. A crane fly, an insect that has been proven to be aerodynamically efficient at low-speed flight, is chosen to perform a characterization and analysis of its structural dynamic response. The internal and external morphologies of the wing are captured and studied using a micro-computed tomography scan. A finite element model is developed from the reconstructed model of the scan for the natural frequencies and mode shapes of the crane fly forewing in vacuum. Furthermore, a fluid-structure interaction model is developed by coupling a finite element model with a computational fluid dynamics model to investigate the deformations of the crane fly forewing under steady and unsteady airflows. The following conclusions are drawn from this study:

1) Micro-computed tomography proves to be a powerful technique to characterize the internal and external structures of complex specimens. Highly accurate measurements of the wing geometry are determined from the reconstructed 2-D cross-sectional images and the corresponding 3-D model. The structure of the wing is characterized by an uniform thickness membrane attached to a venation system formed by tubular veins of two

different thicknesses that take into account the stiffness variation along the spanwise *y*-direction of the wing.

2) The modal characterization of the crane fly forewing indicates that the natural frequency increases with mode and that the mode shapes are highly dominated by bending and torsional deformation responses. For the crane fly forewing, the first four mode shapes are sufficient to describe the structural response as it is highly unlikely that the wing would naturally experience forces that cause vibrations in the order of magnitude of the frequencies from higher modes. Furthermore, the aforementioned deformation responses provide an insight of the stiffness distribution of the crane fly forewing with slightly more flexible regions at the tip of the wing and at the middle of the leading and trailing edge.
3) The deformation magnitude is highly dominated by the out-of-plane deformation, namely the *z*-component of displacement. Furthermore, the deformation along the span of the wing increases nonlinearly from the root to the tip of the wing as the freestream velocity is increased for both steady and unsteady airflow conditions. Such behavior is due to the stiffness provided at the root of the wing by the fixed constraint and by the thick veins. This stiffness gradually decreases along the span of the wing; therefore, it supports the theory that the veins are indeed more than circulatory medium for the wing but also an important structural feature. Moreover, the presence of a nonlinear deformation distribution suggests that the stiffness variation along the spanwise *y*-direction of the wing plays an important role when generating the desired elastic deformations that are well known to enhance the lift capability of insects. In other words, stiffness variation, accounted by the different thicknesses within the venation pattern, serves as the passive regulatory mechanism for the deformation experienced by insects during flight.

REFERENCES

[1] White, F., *Fundamental of Fluid Mechanics,* McGraw-Hill Companies, Inc., New York, USA, 2011.

[2] Nguyen, T., and Byun, D., "Two-Dimensional Aerodynamic Model of Insect Flight for Robotic Flapping Wing Mechanisms of Maximum Efficiency," *Journal of Bionic Engineering,* Vol. 5, No. 1, 2008, pp. 1–11.

[3] Sane, S., "The Aerodynamics of Insect Flight," *The Journal of Experimental Biology*, Vol. 206, No.1, 2003, pp. 4191–4208.

[4] Klowden, M.J., *Physiological systems in Insects,* Academic Press, London, 2013.

[5] McMichael, J.M., and Francis M.S., "Micro Air Vehicles-Towards a New Dimension in Flight," DARPA Technical Paper 1140, 1997.

[6] Pines, D.J., and Felipe B., "Challenges Facing Future Micro-Air-Vehicle Development," *Journal of Aircraft*, Vol. 43, No. 2, 2006, pp. 290–304.

[7] Ellington, C. P., "The Aerodynamics of Hovering Insect Flight. I. The Quasi-Steady Analysis," *Philos. Trans. R. Soc. Lond. B, Biol. Sci.,* Vol. 305, No. 1122, 1984, pp. 1–15.

[8] Ellington, C. P., "The Aerodynamics of Hovering Insect Flight. II. Morphological parameters," *Philos. Trans. R. Soc. Lond. B, Biol. Sci.,* Vol. 305, No. 1122, 1984, pp. 17–40.

[9] Ellington, C. P., "The Aerodynamics of Hovering Insect Flight. III. Kinematics," *Philos. Trans. R. Soc. Lond. B, Biol. Sci.,* Vol. 305, No. 1122, 1984, pp. 41–78.

[10] Ellington, C. P., "The Aerodynamics of Hovering Insect Flight. IV. Aerodynamic Mechanisms," *Philos. Trans. R. Soc. Lond. B, Biol. Sci.,* Vol. 305, No. 1122, 1984, pp. 79–113.

[11] Ellington, C. P., "The Aerodynamics of Hovering Insect Flight. V. Vortex Theory," *Philos. Trans. R. Soc. Lond. B, Biol. Sci.,* Vol. 305, No. 1122, 1984, pp. 115–144.

[12] Ellington, C. P., "The Aerodynamics of Hovering Insect Flight. VI. Lift and Power Requirements," *Philos. Trans. R. Soc. Lond. B, Biol. Sci.,* Vol. 305, No. 1122, 1984, pp. 145–181.

[13] Weis-Fogh, T., "Biology and physics of locust flight. I. Basic principles in insect flight. A critical review," *Phil. Trans. R. Soc. Lond. B.,* Vol. 239, 1956, pp. 415–458.

[14] Weis-Fogh, T., "Quick estimates of flight fitness in hovering animals, including novel mechanisms for lift production," *The Journal of Experimental Biology*, Vol. 59, 1973, pp. 169–230.

[15] Ennos, A.R., and Wootton, R.J., "Functional Wing Morphology and Aerodynamics of *Panorpa Germanica* (Insecta: *Mecoptera*)," *The Journal of Experimental Biology*, Vol. 143, 1989, pp. 267–284.

[16] Wootton, R.J., "Functional Morphology of Insect Wings," *Annual Review of Entomology,* Vol. 37, 1992, pp. 113–40.

[17] Wootton, R.J., "Leading Edge Section and Asymmetric Twisting in the Wings of Flying Butterflies (Insecta, Papilionoidea)," *The Journal of Experimental Biology*, Vol. 180, 1993, pp. 105–117.

[18] Yin, B., and Luo, H., "Effect of Wing Inertia on Hovering Performance of Flexible Flapping Wings," *Physics of Fluids,* Vol. 22, 2010, pp. 111902-1–111902-10.

[19] Combes, S.A., and Daniel, T.L., "Flexural Stiffness in Insect Wings I. Scaling and the Influence of Wing Venation," *The Journal of Experimental Biology,* Vol. 206, No.1, 2003, pp. 2979–2987.

[20] Combes, S.A., and Daniel, T.L., "Flexural Stiffness in Insect Wings II. Spatial Distribution and Dynamic Wing Bending," *The Journal of Experimental Biology,* Vol. 206, No.1, 2003, pp. 2989–2997.

[21] Ishihara, D., Horie, T., and Denda, M., "A Two-Dimensional Computational Study on the Fluid-Structure Interaction Cause of Wing Pitch Change in Dipteran Flapping Flight," *The Journal of Experimental Biology,* Vol. 212, 2009, pp. 1–10.

[22] Combes, S.A., and Daniel, T.L., "Into Thin Air: Contributions of Aerodynamic and Inertial-Elastic Forces to Wing Bending in the Hawkmoth Manduca Sexta," *The Journal of Experimental Biology,* Vol. 206, No.1, 2003, pp. 2999–3006.

[23] Sims, T. W., Palazotto, A.N., and Norris, A., "A Structural Dynamic Analysis of a Manduca Sexta Forewing," *International Journal of Micro Air Vehicles,* Vol. 2, No. 3, 2010, pp. 119–140.

[24] Jongerius, S.R., and Lentink, D., "Structural Analysis of a Dragonfly Wing," *Experimental Mechanics,* Vol. 50, No. 9, 2010, pp. 1323–1334.

[25] Rubio, J., Schilling, P., and Chakravarty, U., "Structural Dynamic Analysis of a Crane Fly Forewing," Proceedings of 55th AIAA/ASME/ASCE/AHS/ASC Structure, Structural Dynamics, and Materials Conference, AIAA Paper No. 2014–1517, National Harbor, MD, January 13-17, 2014.

[26] Ellington, C.P., "The Novel Aerodynamics of Insect Flight: Applications to Micro Air Vehicles," *The Journal of Experimental Biology,* Vol. 202, No.1, 1999, pp. 3439–3448.

[27] Chakravarty, U.K., "Modal Analysis of a Composite Wing of a Micro Air Vehicle," *Journal of Aircraft*, Vol. 48, No. 6, 2011, pp. 2175–2178.

[28] Chakravarty, U.K., and Albertani, R., "Modal Analysis of a Flexible Membrane Wing of Micro Air Vehicles," *Journal of Aircraft,* Vol. 48, No. 6, 2011, pp. 1960–1967.

[29] Wu, P., Stanford, B.K., Sallstrom, E., Ukeiley, L., and Ifju, P.G., "Structural Dynamics and Aerodynamics Measurements of Biologically Inspired Flexible Flapping Wings," *Bioinspiration and Biomimetics,* Vol. 6, No.1, 2011, pp. 1–20.

[30] Coe, R., Freeman, P., Mattingly, P., "Handbooks for the Identification of British Insects. Nematocera: families Tipulidae to Chironomidae (Tipulidae)," *Royal Entomology Society of London,* Vol. 9, No.2, 1950, pp. 1–5.

[31] Ketcham, R.A., and Carlson, W.D., "Acquisition, optimization, and interpretation of X-ray computed tomographic imagery: applications to the geosciences," *Computers and Geosciences,* Vol. 27, No.1, 2001, pp. 381–400.

[32] SkyScan, *Desktop X-ray Microtomography: Skyscan 1172 Instruction Manual*, SkyScan N.V., 2005.

[33] Feldkamp, L.A., Davis, L.C., and Krees, J.W., "Practical Cone-Beam Algorithm," *Journal of the Optical Society of America*, Vol. 1, No. 6, 1984, pp. 612–619.

[34] Chapman, R.F., Simpson, S.J., and Douglas, A.E., *The Insects: Structure and Function*, Cambridge University Press, New York, USA, 2013.

[35] Abaqus 6.12®, Finite Element Analysis Software and User Manual, SIMULIA, Rising Sun Mills, 166 Valley Street, Providence, RI 02909-2499, USA, 2011, <www.simulia.com>.

[36] Agrawal, A., and Agrawal, S., "Design of Bio-inspired Flexible Wings for Flapping-Wing Micro-sized Air Vehicle Applications," *Advanced Robotics*, Vol. 23, No. 6, 2009, pp. 979–1002.

[37] Wainwright, S., Biggs, W., Currey, J., and Gosline, J., *Mechanical Design in Organisms*, Princeton University Press, New Jersey, 1986.

[38] Smith, C., Herbert, R., Wootton, R., and Evans, K., "The Hind wing of the Desert Locus (Schistocerca gregaria*)* II. Mechanical Properties and Functioning of the Membrane," *The Journal of Experimental Biology,* Vol. 203, No. 1, 2000, pp. 2933–2943.

[39] Dudley, R., *The Biomechanics of Insect Flight: form, function, evolution,* Princeton University Press, London, 2002.

[40] Park, J.H., and Yoon, K.J., "Designing a Biomimetic Ornithopter Capable of Sustained and Controlled Flight," *Journal of Bionic Engineering*, Vol. 5, 2008, pp. 39–47.

[41] Wang Z.J., "Dissecting Insect Flight," *Annu. Rev. Fluid Mech.,* Vol. 37, 2005, pp. 183–210.

[42] Tang, J., Viieru, D., and Shyy W., "Effects of Reynolds Number and Flapping Kinematics on Hovering Aerodynamics," *AIAA Journal*, Vol. 46, No. 4, 2008, pp. 967–975.

[43] Inman, D.J., *Engineering Vibration*, Pearson Education Inc., New Jersey, USA, 2007.

[44] White, F., *Viscous Fluid Flow*, McGraw-Hill Companies, Inc., New York, USA, 1991.

[45] Gutierrez, J., Meneses, M., and Chavez, C., "Mathieu Functions, A Visual Approach," *American Journal of Physics*, Vol. 71. No. 3, 2003, pp. 233–242.

VITA

Mr. José E. Rubio was born in Tegucigalpa, Honduras. He completed his B.Sc. in Mechanical Engineering at the University of New Orleans in December 2012. Currently, he is about to finish his M.Sc. in Mechanical Engineering in December 2014 while simultaneously being a Ph.D. candidate in Engineering and Applied Sciences program at the University of New Orleans. He holds a Graduate Assistantship through which he conducts research in the areas of fluid-structure interaction and the design of biologically inspired structures.